Seismic tomography and deformation modeling of the junction of the San Andreas and Calaveras faults

Catherine Dorbath[1]

Ecole et Obervatoire de Physique du Globe - URA 1356 CNRS, Strasbourg, France

David Oppenheimer

U.S.Geological Survey, Menlo Park, California

Falk Amelung and Geoffrey King

Ecole et Obervatoire de Physique du Globe - URA 1356 CNRS, Strasbourg, France

Abstract. Local earthquake P traveltime data is inverted to obtain a three-dimensional tomographic image of the region centered on the junction of the San Andreas and Calaveras faults. The resulting velocity model is then used to relocate more than 17,000 earthquakes and to produce a model of fault structure in the region. These faults serve as the basis for modeling the topography using elastic dislocation methods. The region is of interest because active faults join, it marks the transition zone from creeping to locked fault behavior on the San Andreas fault, it exhibits young topography, and it has a good spatial distribution of seismicity. The tomographic data set is extensive, consisting of 1445 events, 96 stations, and nearly 95,000 travel time readings. Tomographic images are resolvable to depths of 12 km and show significant velocity contrasts across the San Andreas and Calaveras faults, a low-velocity zone associated with the creeping section of the San Andreas fault, and shallow low-velocity sediments in the southern Santa Clara valley and northern Salinas valley. Relocated earthquakes only occur where $v_p > 5$ km/s and indicate that portions of the San Andreas and Calaveras faults are non vertical, although we cannot completely exclude the possibility that all or part of this results from ray tracing problems. The new dips are more consistent with geological observations that dipping faults intersect the surface where surface traces have been mapped. The topographic modeling predicts extensive subsidence in regions characterized by shallow low-velocity material, presumably the result of recent sedimentation. Some details of the topography at the junction of the San Andreas and Calaveras faults are not consistent with the modeling results, suggesting that the current position of this "triple junction" has changed with time. The model also predicts those parts of the fault subject to contraction or extension perpendicular to the fault strike and hence the sense of any dip-slip component. In each locality the relative vertical motion accross the fault is consistent with the fault dips found with the new hypocentral locations.

Introduction

In California, the North American Pacific Plate boundary consists of a network of mostly right-lateral strike-slip faults that collectively accommodate most of the relative motion. The San Andreas is the dominant fault south of the Gabilan Range in central California, whereas farther north, the system in addition includes the Sargent, Calaveras and Vergales faults and several smaller and seismically active faults. The change from the relative simple San Andreas to the more complex set of faults occurs near Hollister and San Juan Bautista, where the San Andreas and Calaveras faults meet in a "triple junction" configuration (Figure 1).

In recent years it has become clear that the topography of a region and the motion on active faults are related. Not only do dipping faults contribute directly to topography, but strike-slip motion on vertical faults can generate local changes in topography where fault geometry is complex. Although many faults can be mapped from their surface expression, blind faults may exist as well as features that are not well represented by surface mapping. Moreover, the detailed geometry of those already identified is often poorly known. A major source of information, which can be directed to improving our understanding, resides in the seismic data. Seismicity studies provide both fault orientation and sense of motion, and seismic tomography can also reveal through velocity variations the extent of sedimentary basins. In this paper we analyze the seismicity of the Hollister region to obtain a three-dimensional (3-D) velocity model and improved locations of earthquakes using local earthquake tomography.

The region of the study is particularly favorable for seismic tomography. The seismicity is conveniently distributed in the area, largely as a result of the very complexity we wish to study. The San Andreas and Calaveras faults diverge with a 30°

[1]Also at ORSTOM, Institut Français de Recherche Scientifique pour le Développement en Coopération, Paris, France.
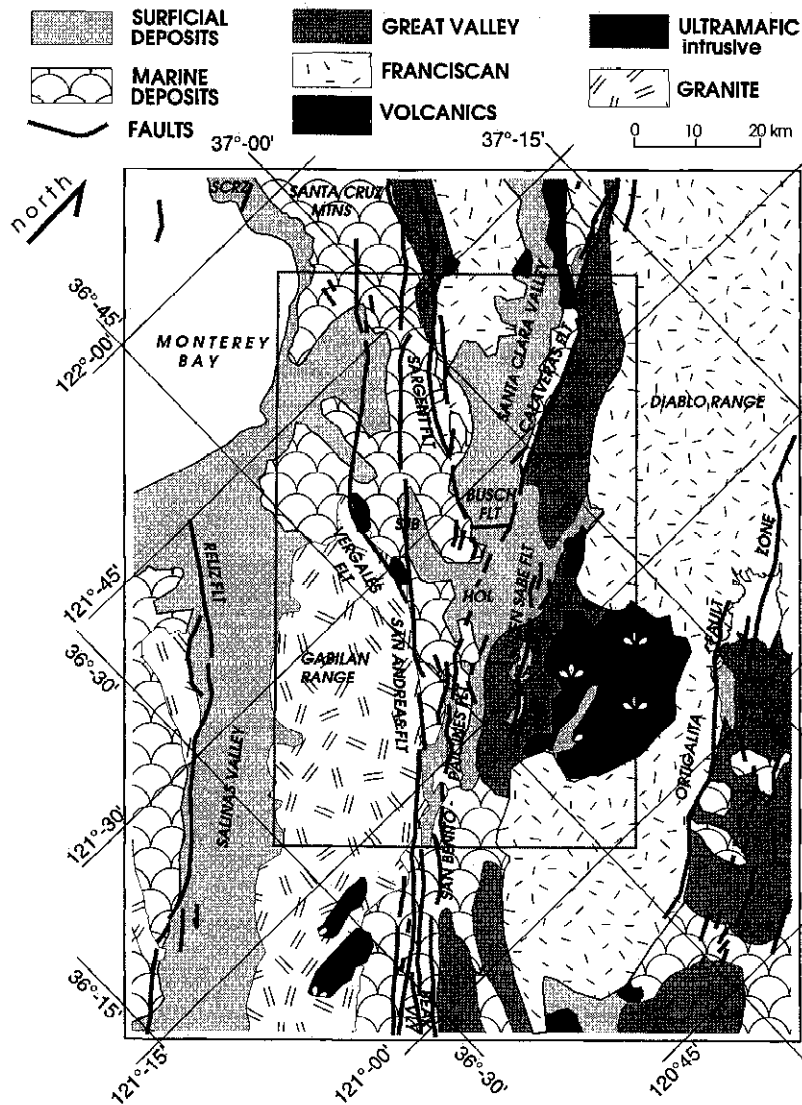
Figure 1. Generalized geology and fault map of study region. The rectangular box defines area imaged by tomographic inversion. Abbreviations are: FLT, fault; HOL, Hollister; MTNS, mountains; SA VLY, Santa Anna Valley; SCRZ, Santa Cruz; SJB, San Juan Bautista; VLY, valley.

angle, and smaller active faults with various orientations leave few regions devoid of earthquakes (Figure 2). The numerous stations of the Northern California Seismic Network (NCSN) operated by the U.S. Geological Survey provide data for a 27-year period, such that an excellent distribution of ray paths is available.

Parts of the region that we examine have been studied before. In most cases, if not all cases, we consider that the velocity models and earthquake locations we provide are better than earlier efforts. However, the main object of studying a large region is not to improve upon these detailed earlier studies. The purpose is to provide a global view of a tectonically significant region in a form that can be used to understand active tectonic processes better. The consistency of our results with earlier studies, which have employed different ray tracing methods and inversion algorithms, gives us reason to believe that our results are to be trusted.

To illustrate an application of our results, we use them to refine the fault geometry in the Hollister region. Thiss in turn is used to model the topography of the Hollister region using elastic dislocation theory.

Structural Setting

In central California the San Andreas fault is a boundary between the Salinian block to the west and the Franciscan assemblage and overlying strata of the Great Valley sequence to the east (Figure 1). In the region under study the Franciscan formation, composed of metamorphosed sedimentary and volcanic rocks, is largely present to the east of the Calaveras fault in the Diablo range, an antiform surrounded by Great Valley sequence rocks. It also outcrops in the Santa Cruz mountains to the east of the Sargent fault. The Gabilan range, to the west of the San Andreas fault, consists of granitic and metamorphic rocks of the Salinian block. The central part of the studied area is filled by Tertiary and Quaternary sediments in the Santa Clara valley, the northern Salina valley, and Bear valley (Figure 1).

In the area of study the patterns of seismicity differ markedly along the San Andreas fault. To the south of San Juan Bautista, the fault is characterized by aseismic slip (creep) [*Simpson*, 1994; *Savage et al.*, 1979] and frequent small-magnitude earthquakes. To the north, the San Andreas fault is
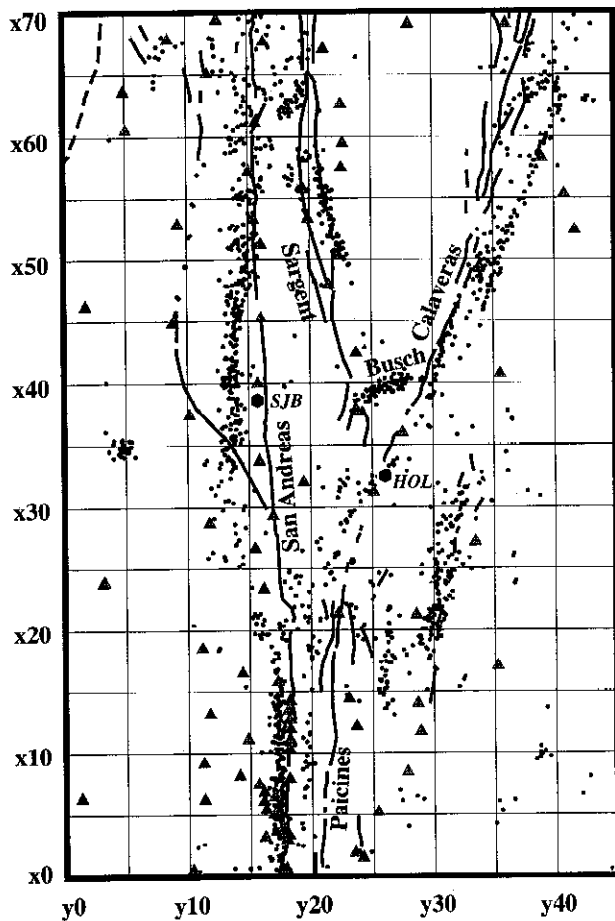
Figure 2. Map of epicenters (circles), seismic stations (triangles), and model grid spacing used in tomographic study in Hollister area. The 1445 events used in the study were selected from a set of 17,000 events to provide a uniform source distribution in three dimensions. The 3-D velocity values are calculated at the intersection points (nodes) of the equally spaced, 5-km, horizontal grid. The vertical grid spacing is 3 km. Region corresponds to rectangular box in Figure 1. Select faults are labeled. Abbreviations are: HOL, Hollister, SJB, San Juan Bautista.

characterized by less frequent earthquakes, some of which are of large magnitude; creep has never been measured. This part of the fault was associated with rupture both in the great 1906 (M=7.8) earthquake, and the 1989 Loma Prieta (M=7.0) earthquake. Creep also occurs along the Calaveras fault and the southern part of Sargent fault. Although subject to creep, segments of these faults have produced moderate earthquakes, the most recent being the 1979 Coyote Lake (M=5.7) and the 1984 Morgan Hill (M=6.2) earthquakes, which ruptured adjacent segments of the Calaveras fault. The differing mechanical behavior of the different segments is manifest through the seismicity which occurs on the faults. The creeping segments of the fault are characterized by concentrations of small earthquakes [Oppenheimer et al., 1990], while locked segments show sparse, if any, seismicity. Cross sections transverse to the fault system by Hill et al. [1990] show creeping faults to have a near vertical hypocenter distribution (80° to 90° dip) and a uniform depth of about 15 km to the base of the seismogenic zone. The Salinian block is relatively devoid of seismicity compared to the Franciscan terrane.

Studies of the crustal and upper mantle structure along the San Andreas fault system have been conducted for more than half a century. Seismic refraction profiles have been interpreted by Walter and Mooney [1982], Blümling and Prodehl [1983], Blümling et al. [1985], and Mooney and Colburn [1985]. The area is crossed by the Centennial Continent-Ocean Transect C2 [Saleeby, 1986]. Fuis and Mooney [1990] reinterpreted the available seismic refraction data to construct a crustal cross section for central California. One- and three-dimensional velocity models have also been deduced from earthquake travel times for Loma Prieta [Dietz and Ellsworth, 1990; Eberhart-Phillips et al., 1990; Lees and Shalev, 1992; Foxall et al., 1993], Morgan Hill [Cockerham and Eaton, 1987; Michael, 1988, Lin and Roecker, preprint, 1994a], Bear Valley [Aki and Lee, 1976, Lin and Roecker, preprint, 1994b], and the Coyote Lake area [Thurber, 1983]. None of this earlier work covers the whole of our study area, but nonetheless, in several regions we can compare our velocity models with independent studies.

Tomographic Inversion

We simultaneously inverted earthquake travel time data from local earthquakes to determine both the locations of earthquakes and the 3-D seismic velocity structure of the Earth beneath the seismic array. The damped least squares technique we use for simultaneous inversion was originally developed by Thurber [1983] and was first applied to the Coyote Lake area. The method has been applied to numerous earthquake source regions and is fully described by Eberhart-Phillips [1990], Thurber [1993], and Eberhart-Phillips [1993].

The arrival times used in this study were obtained from the Northern California Earthquake Data Center [Romanocwicz et al., 1994]. The first dense network of seismic stations were installed in this region by the U.S. Geological Survey in 1967, and there have been more than 17,000 events located in the study area by the NCSN in the subsequent 27 years. For the inversions we chose events using restrictive criteria to retain only the best quality data. We first selected the events meeting the following criteria: RMS < 0.20 s, horizontal standard error < 1.5 km, vertical standard error < 2.5 km, magnitude > 2.0, number of stations > 30. Then we eliminated earthquakes with similar locations, keeping only the best located events within cells with dimensions of 0.5 km per side. The final data set, shown in Figure 2, consists of 1445 events concentrated primarily on the active faults but also distributed throughout the region.

There are 96 stations located within the study area (Figure 2), among which 42 belonged to temporary networks deployed in Bear Valley during a 6-month period in the second half of 1974. Although these temporary stations provide only a small part of the data, they improve the resolution of the inversion in a region with strong lateral velocity gradients. Slightly more than 50% of the permanent stations (26 stations) recorded between 75 and 100% of the selected events. In addition, 133 stations located outside the area imaged by tomography were used only to improve the reliability of hypocentral relocations. The data set includes 94,806 travel times, of which nearly all are initial P wave arrival times. Since only 27 stations record three components, relatively few reliable S readings (2258) are available. Although the S travel times are insufficient to obtain an S velocity model, they constrain hypocentral depths and hence improve the tomography.

Table 1. Gradient P Velocity Models

Location	Reference	Z, km	V, kn/s
Coyote Lake (COY)	*Reasenberg and Ellsworth* [1982]	0.00	3.80
		1.40	5.30
		5.80	6.12
		10.60	6.37
		24.00	6.59
		27.00	8.00
Bear Valley			
Diablo Range side (DIA)	*L. Dietz* (personal communication, 1996)	0.00	2.45
	and *Walter and Mooney* [1982]	1.50	4.62
		5.80	5.80
		14.40	6.05
		15.60	6.85
		29.00	7.15
		31.00	7.95
Gabilan Range side (GAB)	*L. Dietz* (personal communication, 1996)	0.00	3.73
	and*Walter and Mooney* [1982]	4.00	6.07
		22.50	6.47
		25.50	7.95
Loma Prieta			
Pacific side (LOM)	*Dietz and Ellsworth* [1990]	0.00	3.00
		2.00	4.95
		6.70	5.94
		24.00	6.64
		26.00	8.00
North American side (LON)	*Dietz and Ellsworth* [1990]	0.00	2.53
		2.50	5.44
		8.90	6.29
		24.00	6.69
		26.00	7.98
Default Northern California (NCG)	*J. Eaton* (personal communication, 1996)	0.00	2.70
		3.50	5.70
		23.00	6.80
		27.00	8.05
Tres Piños (TRE)	*L. Dietz* (personal communication, 1996)	0.00	2.70
	and*Walter and Mooney* [1982]	2.00	5.33
		5.60	5.75
		14.40	6.00
		16.00	6.83
		28.40	7.07
		30.00	7.95

In *Thurber's* [1983] inversion method the velocity structure is parametrized by assigning velocity values at discrete points of a 3-D grid and linearly interpolating between these points. The study zone is a rectangular region 45 by 70 km, the x axis has an azimuth of 46° eas of north such that it aligns with the average strike of the San Andreas fault in the region. To accommodate the complex geometry of the fault system, we used a regular 5-km horizontal grid spacing (Figure 2). This regular grid does not emphasize a priori any particular feature, although it is orientated to resolve a velocity contrast across the San Andreas fault. The model extends to a depth of 15 km, the maximum depth of seismicity, with a vertical grid spacing of 3 km.

The initial velocities at the grid nodes were adopted from four different one-dimensional P velocity models used by the NCSN for routine earthquake location (Table 1 and Figure 3) [*Dietz and Ellsworth*, 1990; *Reasenberg and Ellsworth*, 1982; *Walter and Mooney*, 1982]. Two models have different velocity profiles on either side of the San Andreas fault: Loma Prieta (LOM/LON) and Bear Valley (GAB/DIA). The velocities of regions falling between models were interpolated between the closest models. Some other studies start from the best

initial 1-D model. However, like *Eberhart-Philips* [1990] or C.H. Lin and S.W. Roecker [preprint, 1994], we consider it more appropriate to start from the best available well-tested model rather than create one ourselves.

We calculated station corrections only for stations outside the tomography area. Distant stations improve hypocenter stability by improving ray path distribution. Simultaneous inversion for velocity structure, but with hypocenter delays only for distant stations, has been shown to be an effective method that reduces contamination of the modeled velocity structure by velocity variations occurring outside the model [*Eberhart-Phillips*, 1993]. After calculating the 3-D model, we inverted for the station delays relative to the final model to account for local travel time variations that could not be represented by the coarse grid spacing of the model. The delays and final 3-D model were used in the relocation of the entire set of 17,341 earthquakes.

We conducted a series of tests to determine the selection of the grid spacing and origin. All the grids tested were more closely spaced than those used by previous workers (except very close to the fault) and regularly spaced everywhere. No attempt was made to specify the fault location except that the
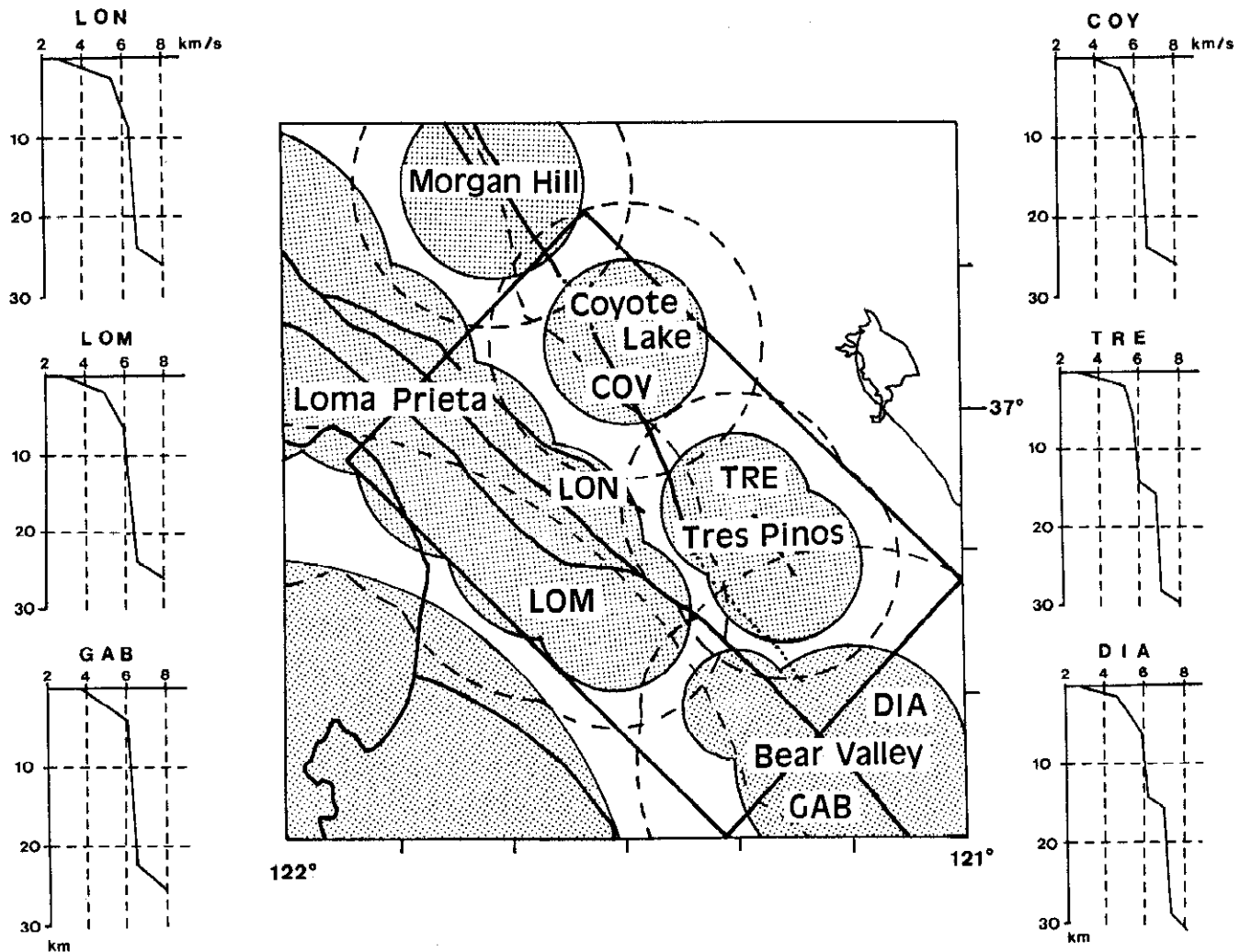
Figure 3. The NCSN velocity models used to determine the initial earthquake locations for tomographic inversion. Shaded regions depict boundaries of models. Earthquakes occurring outside models but within dashed regions have locations based on a combination of adjoining models. Velocity (abscissa) versus depth (ordinate) profiles of models, denoted by a three-letter code are shown in margins. Earthquakes occurring outside dashed lines are located by the default (NCG) velocity model. The rectangular box defines area imaged by tomographic inversion. See Figure 1 for names of faults (solid lines).

overall orientation of the grid is parallel to the mean fault direction. From these tests we conclude that the final results are insensitive either to the grid spacing (it is dense enough) or its spatial location. To select the best damping parameter 10 different values between 5 and 1000 were calculated. The one selected was chosen to give the best trade-off between resolution and error. We next assessed the sensitivity of the inversion to the starting model. To create an alternative starting model, we relocated the 1445 selected events with the HYPOINVERSE location program [Klein, 1989] using a simple one-dimensional, four-layered velocity model (NCG) (Table 1) used by the NCSN to locate earthquakes which occur outside regions where improved 1-D models have been determined. The resulting HYPOINVERSE locations differed by as much as 4 km from those computed with one of the four individual models shown in Figure 3. We then inverted the data again, using the NCG velocity model and corresponding hypocenter locations as a starting model. Despite the large difference in the initial locations and model, the epicenters resulting from the

inversion are generally less than 1 km apart from those determined from the multiple initial models, even in those regions where the separation was 4 km. Moreover, the mean P velocity and the pattern of velocity variations in each layer are nearly identical for both models to depths of 12 km. The maximum difference of 6% occurs near the surface where velocity control is minimal in the absence of a nearby station.

We also assessed the effect of S travel time data on the inversion. The P velocity model is insensitive to the presence of S data, but significant differences are observed in the depth of relocated hypocenters. Though the alignment of hypocenters observed in cross sections display the same dips without S data, the scatter of the locations about the presumed fault plane is greater. Finally, a comparison was done with an inversion without any station corrections for the peripheral area. The relocated hypocenters change less than 0.5 km, and the velocity model displays the same general patterns. However, the velocity contrasts are sharper when station corrections are included. In summary, we find that the results
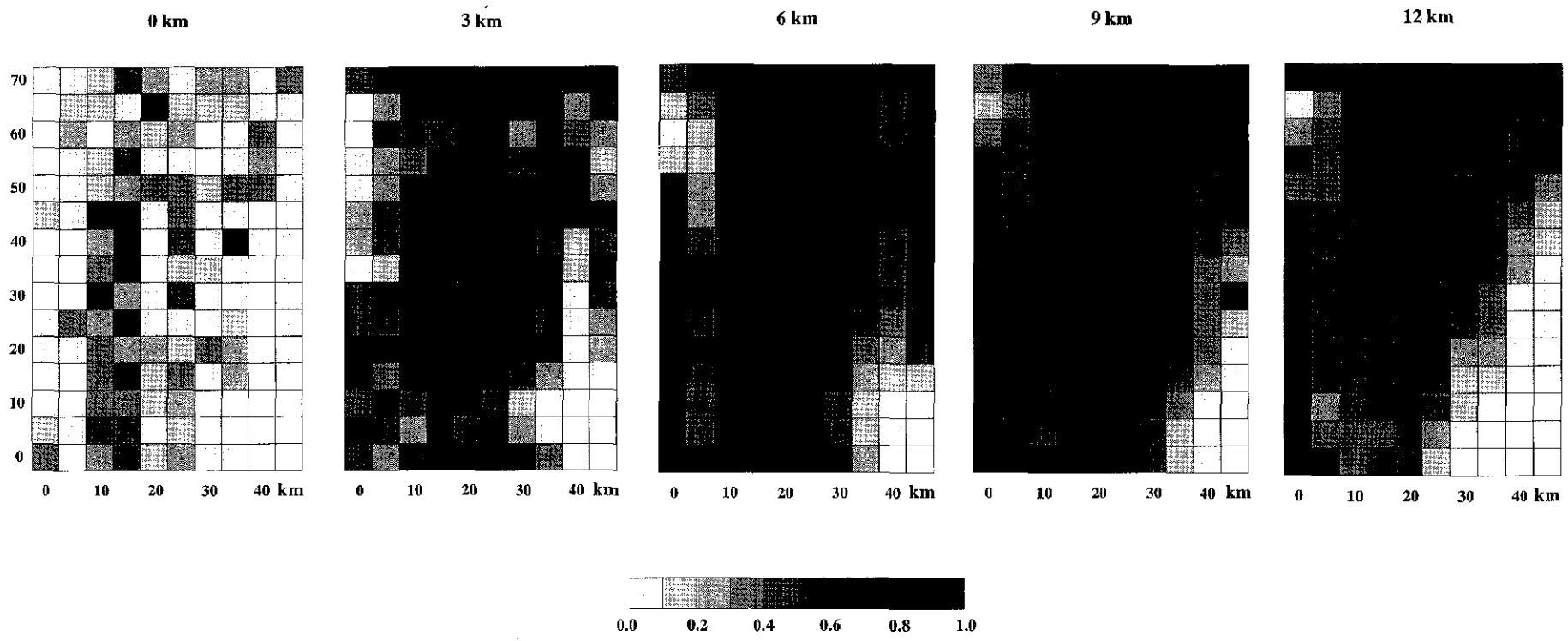
Figure 4. Diagonal elements of resolution matrix for final model. Resolution reflects station spacing and distribution of seismicity. See Figure 2 for location of earthquakes and stations with respect to grid spacing.

we report are robust in that they are generally insensitive to the starting velocity model, initial earthquake locations, presence of S travel time, and the use of station corrections.

Inversion Results

These results were obtained after 6 iterations, resulting in a reduction of the initial P data variance by 84% from 0.14 to 0.02 s^2. The convergence is rapid with a reduction of 80% being obtained after 3 iterations. Figure 4 shows the diagonal elements of the resolution matrix for the five upper layers. The resolution at the surface directly reflects the station distribution and is consequently variable, being high close to stations and low elsewhere. The resolution improves with depth. The central part of the grid is best resolved at any depth. The highest resolution is observed at 6 km and slightly decreases at greater depths but remains higher than 0.5 for the central region down to 12 km. The resolution observed at the border nodes is related to the distribution of peripheral stations with the lowest resolution at any depth being in the east due to the lack of peripheral stations in eastern azimuths. The standard errors of velocity depend on the resolution and the mean velocity. For the nodes for which the diagonal elements of the resolution matrix are greater than 0.5, the error must be 0.1 km/s at the surface and reaches 0.5 km/s at 12 km. The standard errors of the relocations have been calculated for each event and have little systematic dependence on the hypocentral location of the events. The mean horizontal error is 140 m, and the depth error is 240 m.

For higher resolutions the velocity solution is clearly more reliable, and sharp velocity contrasts are resolved better. However, the series of tests described earlier strongly suggests that the velocity solution nonetheless may be trusted even in regions of lower resolution and that our final results are robust such that over much of our grid we are resolving scale lengths of the order of our grid spacing (5 km).

Velocity structure. The velocity solution in the five layers is presented in map view in Figure 5. For 334 of the 1598 velocity nodes the velocity was unresolved due to a lack of ray paths, and we assigned the initial velocity to the node. The most prominent feature observed on the four upper layers is a narrow low-velocity zone bounded to the southwest by the San Andreas fault. In Bear Valley this zone is confined between the San Andreas and the Paicines faults but continues to the north, ending abruptly between the San Andreas fault and the southern segment of the Sargent fault. The body is slightly wider at 9 km depth than at shallower depths, which most likely is due to poorer resolution at depth. Although the body is imaged primarily by one column of nodes ($X=20$), the feature was also imaged when we shift the origin of the grid by one half the grid spacing.

Some velocity patterns are observed only in the first two layers. For example, a prominent high-velocity zone is found at depths above 6 km southwest of the San Andreas fault in the Gabilan range west of Bear Valley. In the central part of the region where the branching of the Calaveras fault occurs, we also observe low velocities at depths shallower than 3 km in the region between the San Andreas and the Calaveras faults. This shallow low-velocity wedge extends to the Busch fault and the southern end of the Sargent fault. It is likely to be associated with Quaternary sediments deposited in the Santa Clara valley (Figure 1). This feature also separates the Diablo Range from the high-velocity Franciscan formation

outcropping in the Santa Cruz Mountains to the northeast of the Sargent fault. On average, the velocities observed in the northeastern part of the study area, within the Franciscan block, are lower than those associated with the Salinian block.

Earthquake locations. Figure 6 shows a comparison between the final epicentral locations (circles) and those located by the NCSN standard procedure. Nearly 56% of the 1445 relocated epicenters differ by less than 1 km from the initial location, 81% by less than 1.5 km and 93% by less than 2 km. The differences in depth are nearly the same with 68% differing by less than 1 km, 86% by less than 1.5 km and 94% by less than 2 km. Despite these modest shifts, the relocations show important differences in trend.

The largest difference is observed along the Calaveras fault where the epicenters are shifted northeast by about 1.7 km. A cross section (Figure 6, FF') perpendicular to the Calaveras fault in its central part shows that the relocated hypocenters are slightly deeper and the horizontal shift increases with depth. The seismicity remains confined between 4 and 10 km as on the original cross section. Unlike the 80° dipping fault zone defined by the NCSN locations whose surface projection is offset from its surface expression, the new locations dip at 70° and project to the surface where the fault is mapped. A similar correlation between the new hypocenters and the mapped fault occurs for the adjacent cross section EE' to the south. In this case, however, the correlation results from a decrease in fault dip from 85° to 75°. In both cases the hypocenters appear less scattered than for the NCSN locations.

Along the San Andreas fault in Bear Valley, the relocated epicenters are shifted to the southwest about 1.5 km. The cross section (Figure 6, AA') again shows a systematic shift with depth. The relocated seismicity defines a very narrow plane dipping about 80° to the southwest, whereas the NCSN locations define a near-vertical plane. The surface projection of the NCSN and relocated seismicity project to the mapped location of the San Andreas fault at the surface. Farther north along the San Andreas fault, the hypocenters are shifted upward by about 1.5 km. For cross section BB' the seismicity which was concentrated between 4 and 10 km defines a narrower plane after relocation within a depth range between 1.5 and 8.5 km. The dip of the fault plane remains unchanged at about 80° and, as for Bear Valley, projects to the surface at the surface trace. Small changes are observed for the cross section CC'. The San Andreas fault plane remains at a dip of about 80° and seismicity locates, as before, from the surface to a depth of 13 km. Since there are a number of nearby stations, the depth determination of this seismicity is presumably well controlled.

The hypocenters associated with the nearby Sargent fault experience greater changes, with average shifts to the south of 1 km and deepen by 1.5 km (Figure 6, DD'). The cross section shows that the fault plane defined by the seismicity is still near-vertical. Although the epicenters are somewhat scattered, the upward projection of the plane is in better agreement with the mapped surface fault, though it still projects 1.5 km northeast of the surface trace. For the Busch fault the relocated epicenters are essentially unchanged from the NCSN epicenters, and the fault plane remains vertical. After relocation, however, activity becomes concentrated between 3 and 9.5 km rather than between 2 and 11 km (Figure 6, HH').

We find that the general pattern of the seismicity in the study area changes modestly, but significantly, after relocation. Comparison of the epicenters in Figures 2 and 6 suggests that in many regions the relocated earthquakes are
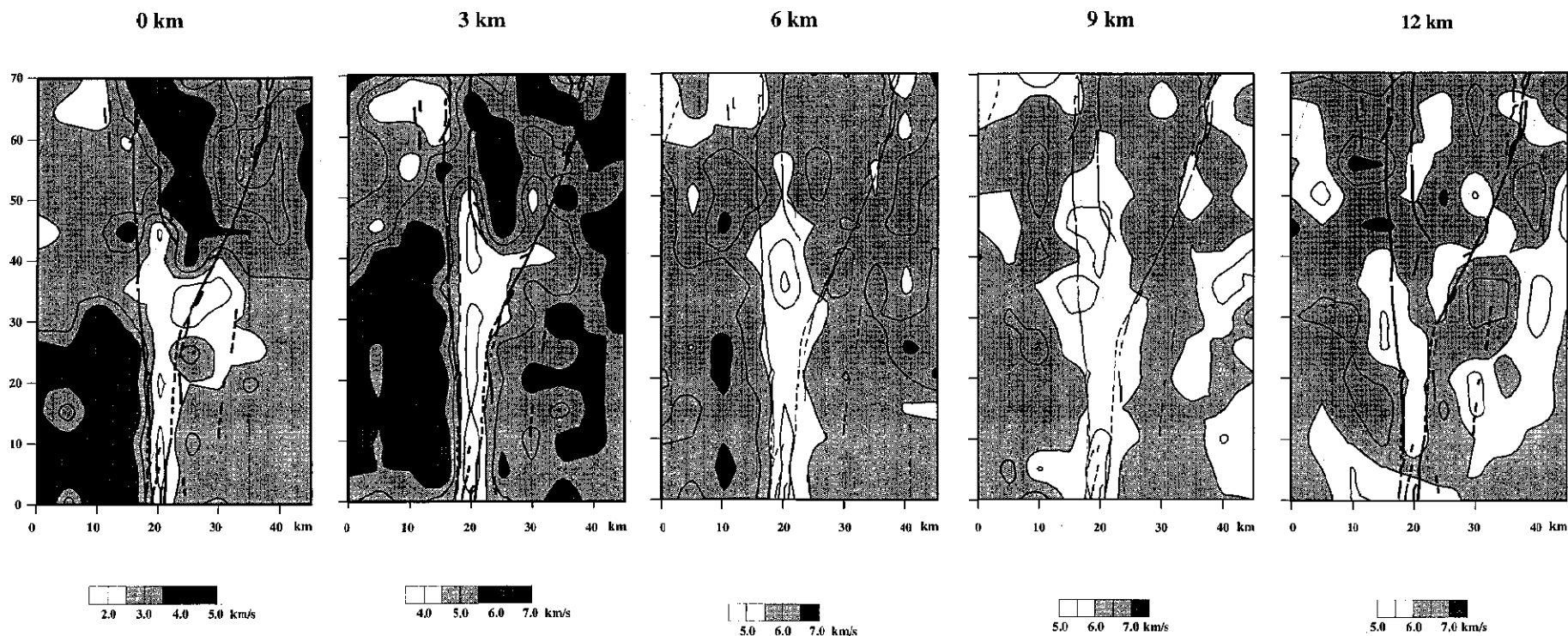
Figure 5. Three-dimensional compression velocity results for final model for Hollister area. The gridded results have been smoothed for purposes of display. Note pronounced low-velocity body between San Andreas and Paicines faults that extends to 9 km. Shallow low-velocity features coincide with northern Salinas valley and southern Santa Clara valley. The Sargent fault coincides with southwest boundary of high velocity body. See Figure 1 for names of faults and Figure 4 for model resolution.
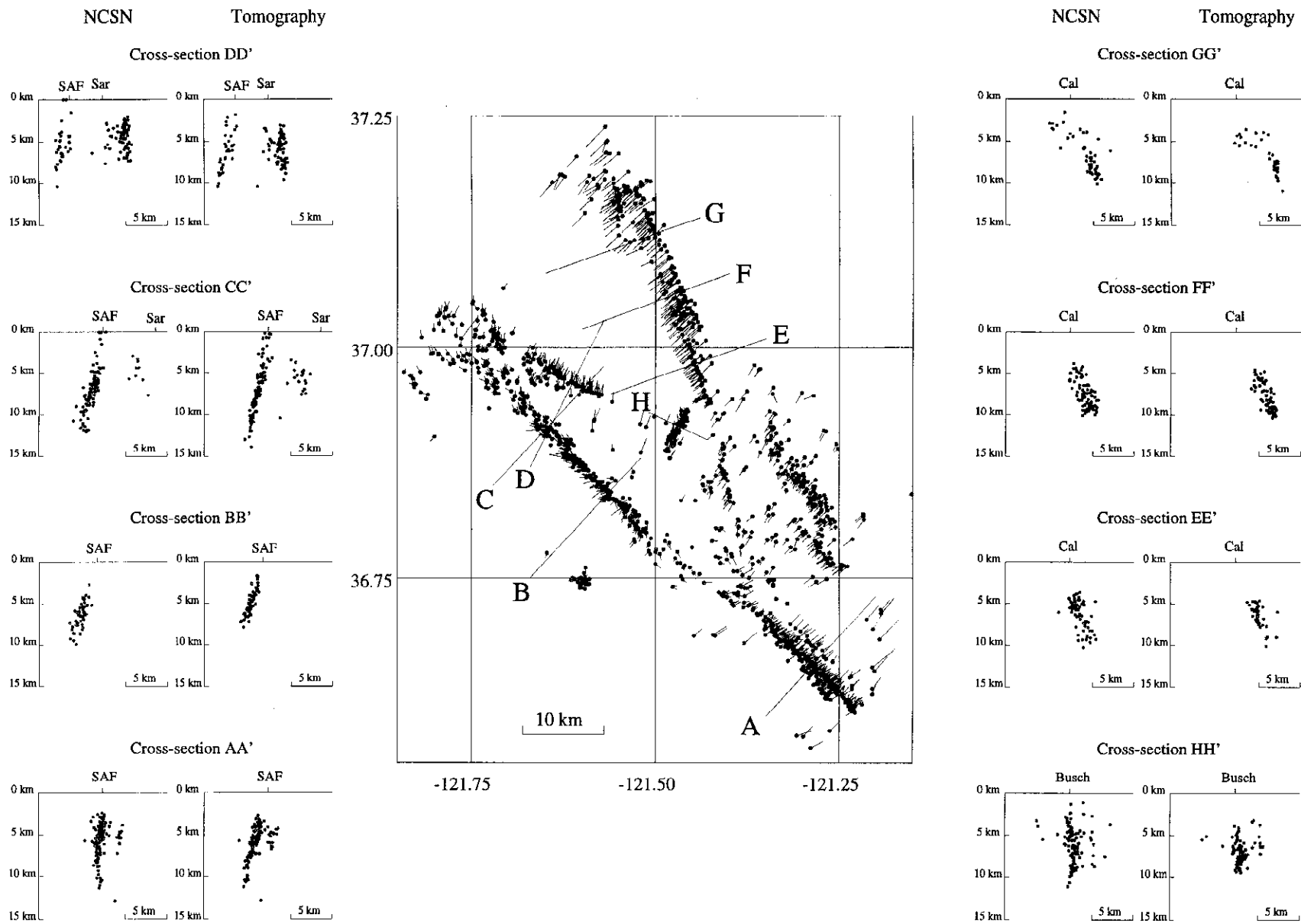
Figure 6. Comparison of the NCSN earthquake locations based on multiple velocity models (Figure 3 and Table 1) with 3-D relocations based on observed travel times and final tomographic velocity model. The stick plots relate the tomographic locations (circles) to the initial locations. The width of the cross sections is 10 km. Abbreviationsare: SAF, San Andreas fault; Sar, Sargent fault; Cal, Calaveras fault; Busch, Busch fault.

more diffuse and farther from the mapped faults. This, however, is an artifact of the projection. In most cases the relocated hypocenters more closely define planes, and those planes project closer to the mapped surface fault traces than before. The relocated epicenters also remove an apparent bend in the San Andreas fault between section AA' and BB'; epicenters to the south are shifted to the northeast bringing them into alignment with those to the north shifted to the southwest. This bend in the 1-D locations probably reflects the boundaries of the different velocity models used in the NCSN location procedure.

Relation between the velocity structure and the relocated hypocenters. In Figure 7 we show 15 new x velocity-depth sections, and the relocated hypocenters, oriented SW-NE perpendicular to the San Andreas Fault and three y velocity-depth sections oriented NW-SE parallel to the SAF. Because of the grid orientation these sections are nearly perpendicular to most structures except for the Calaveras fault. In the northeastern part of the study area the seismicity is relatively diffuse and the velocity contrasts are smooth (Figure 7, x70, x65, and x60). A small increase of the velocity in the upper 5 km occurs from SW to NE across the San Andreas fault. Low superficial velocities are observed to the west of the Calaveras fault. For all the other cross sections (Figure 7, x55 to x0), a marked vertical velocity contrast is associated with the San Andreas fault. The Salinian block is characterized by higher velocities, about 6.0 km/s at a depth of 5 km. Immediately to the east of the seismically defined fault plane, the inversion images velocities as low as 5.0 km/s from the surface to depths of about 5 km in the northern cross-sections (Figure 7, x55 to x45) and to depths of approximately 8 km in sections farther south.

In sections x55 to x45, the high-velocity body east of the Sargent fault beneath the Santa Cruz mountains separates the deep, low-velocity body between the San Andreas and Sargent faults from the more superficial low-velocity body associated with the sediments of the Santa Clara valley. For sections x40 to x30 a shallow low-velocity zone extends between the San Andreas and the Calaveras faults. Farther south (sections x25 to x15) the low-velocity body extends to greater depth and is bounded to the southwest by the seismicity of the San Andreas fault. On the northeast it is bounded by the Paicines fault, which is not defined by the seismicity selected for the inversion. The extent of this low velocity feature is very clearly seen in cross sections parallel to the San Andreas fault (Figure 7, y20).

Discussion

The velocity model. The velocity model found in this study can be compared with results from published seismic refraction studies. The northern portion of our study area (Figure 7, x65 and x60) is crossed by the transect C2 of *Saleeby* [1986], for which *Fuis and Mooney* [1990] reinterpreted the velocity structure. Our cross section x65 and their transect C2 are superimposed in Figure 8. Their lowest velocities are observed directly beneath the San Andreas and Sargent faults (3.34 km/s between 0 and 3 km on C2) and southwest of the Calaveras fault system (2.7 km/s at the surface). These low velocities are likely to be related to the Tertiary sedimentary rocks. Immediately below these sedimentary rocks are rocks with observed velocities between 4.0 and 4.5 km/s related to the presence of late Cretaceous

terrain. At a depth of 5 km the velocity increases from the west to the east (5.45 to 6.0 km/s on C2). Finally, the top of the midcrustal layer defined by a velocity of about 6.35 km/s is reached at about 9 km depth. Thus the velocities and positions of anomalies obtained by travel time inversion are generally consistent with the interpretation of refraction data.

As mentioned earlier, there have been several other tomographic studies performed in central California with regions that overlap, to some extent, with our region of study. In fact, the first application of the inversion method used in this study was performed by *Thurber* [1983] for the Coyote Lake region. As the grid point spacing is nearly the same in both cases, a comparison of the final velocity models is direct. The most obvious feature found by Thurber is a low-velocity wedge extending from the surface to at least 7 km depth between the San Andreas and the Calaveras faults. This body extends only as far north as the creeping zone of the San Andreas, the southern mapped extent of the Sargent fault and the intersection with the Busch and Calaveras faults. Although our model is similar to the Thurber model near the surface, it differs at depths below 3 km. Our low-velocity wedge is a narrow zone that follows the San Andreas fault but does not extend as far east as the Calaveras fault. Moreover, the velocity contrasts are much sharper in our model. We suppose that this is a result of the higher resolution of our model arising from the large number of ray paths.

The first determination of 3-D velocity anomalies using P arrival times from local earthquakes was performed by *Aki and Lee* [1976] at Bear Valley. In the upper 5 km depth interval of their model they found a low-velocity zone of about 5 km/s in the San Andreas fault zone sandwiched between high-velocity areas of about 6 km/s. Within the limits of resolution this is compatible with our result. *Foxall et al.* [1993] also calculated the three-dimensional velocity structure of the southern Santa Cruz Mountains, spanning the northern half (Figure 7, x70 to x40) of our model. Since their method [*Michelini and McEvilly*, 1991] is similar to the method used in this study, their results are essentially identical to those reported here for the region common to both studies. In particular, the slow body seen to the east of the San Andreas to its northern limit has the same velocities (3.6 km/s at 4 km depth and 5 km/s at 9 km). C.H. Lin and S.W. Roecker (preprints, 1994) performed a local tomographic study of a 135 km x 65 km area in the Bear valley region. Our study is located in the northwestern half of their study area. Their initial velocity models, data set, and inversion method are quite different than ours. Their grid spacing is irregular and generally twice as large as the spacing in this study, except in the San Andreas fault zone. The main features, as well as the velocities, however, are essentially the same in the upper layers in both studies. At depths below 6 km we image lower velocities between the San Andreas and Paicines faults. Another difference is that we image a narrow, low-velocity structure to the northeast of the San Andreas fault to depths of at least 6 km, but it is located directly beneath the fault in the Lin and Roecker study.

Finally, the southernmost cross section presented by *Eberhart-Phillips et al.* [1990] may be compared to the cross sections x45 and x40. That study utilized aftershocks of the Loma Prieta earthquake as sources, the same initial velocity model as we used, and a velocity grid spacing of 10 km with denser spacing in the fault zone. The velocity images are essentially identical across the San Andreas fault zone on both models.
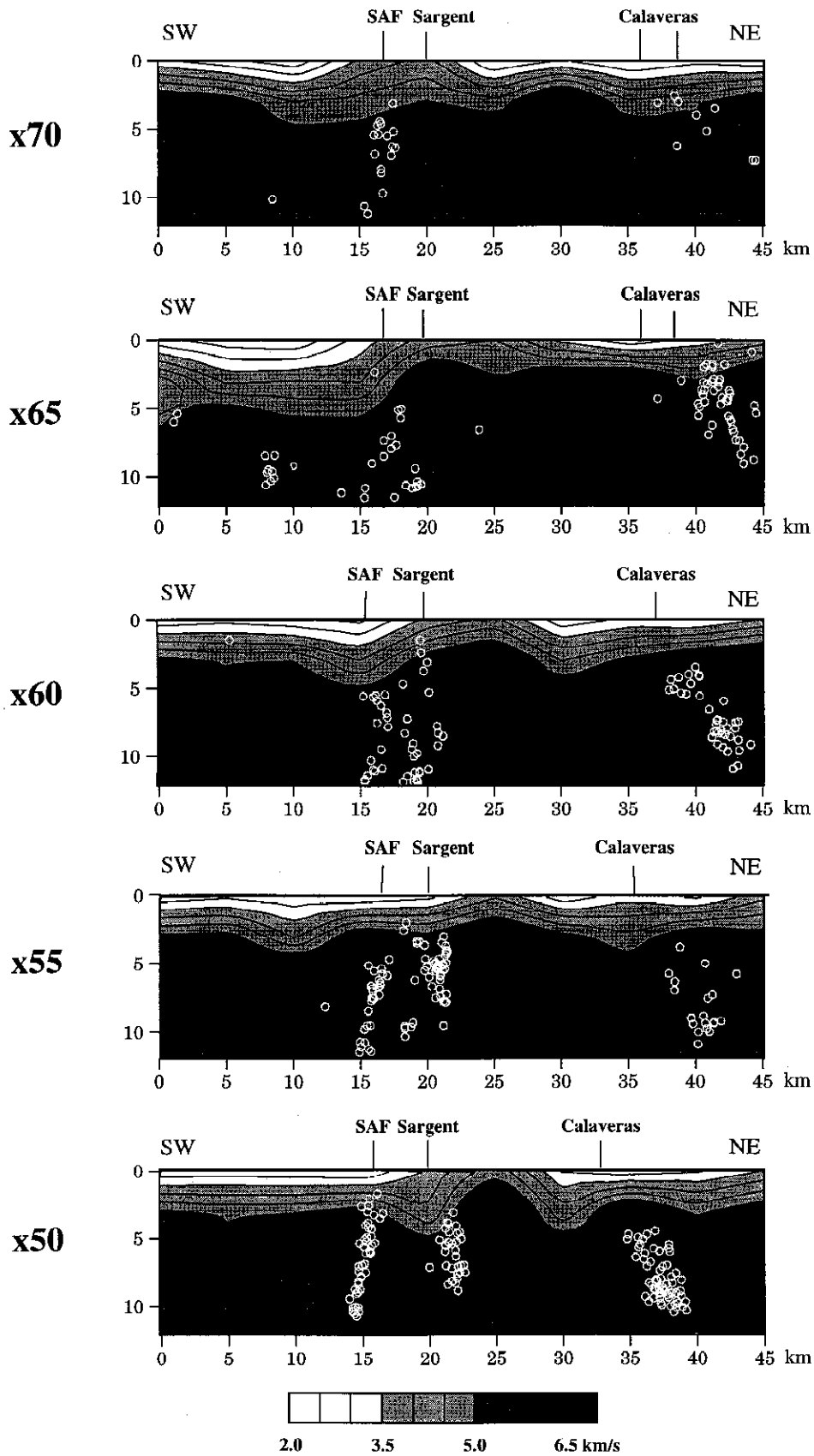
Figure 7a. Cross-sectional view of 1445 earthquakes relocated by tomographic inversion, superimposed on the 3-D velocity images for sections x70 - X50. Key to cross sections is presented on Figure 2. Cross sections are perpendicular to the San Andreas fault. The gridded results have been smoothed for purposes of display. Abbreviations: SJB, San Juan Bautista; H, Hollister; SAF, San Andreas fault; Paicines, Paicines fault; Santa Anna, Santa Anna Valley; Sargent, Sargent fault; Calaveras, Calaveras fault; Busch, Busch fault.
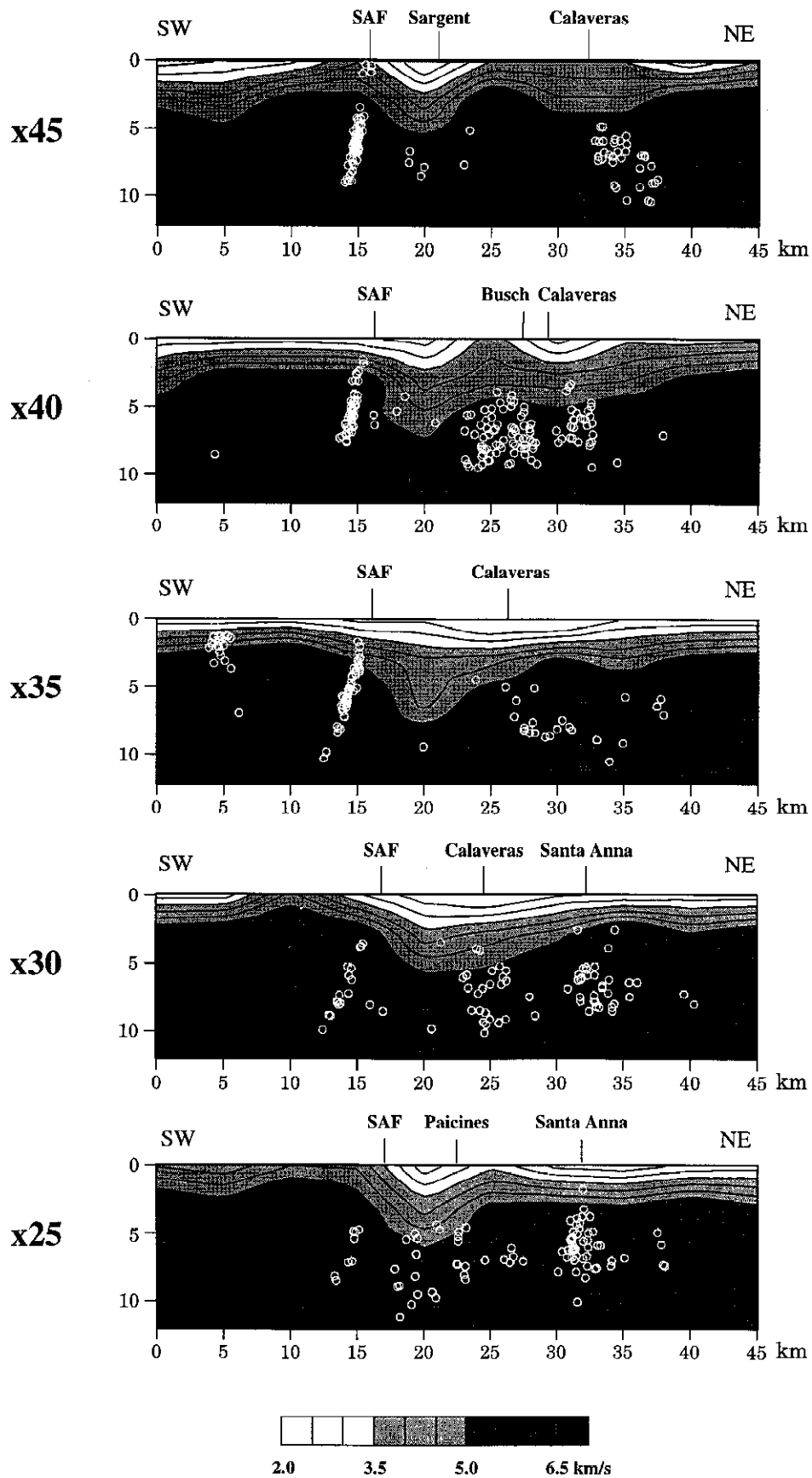
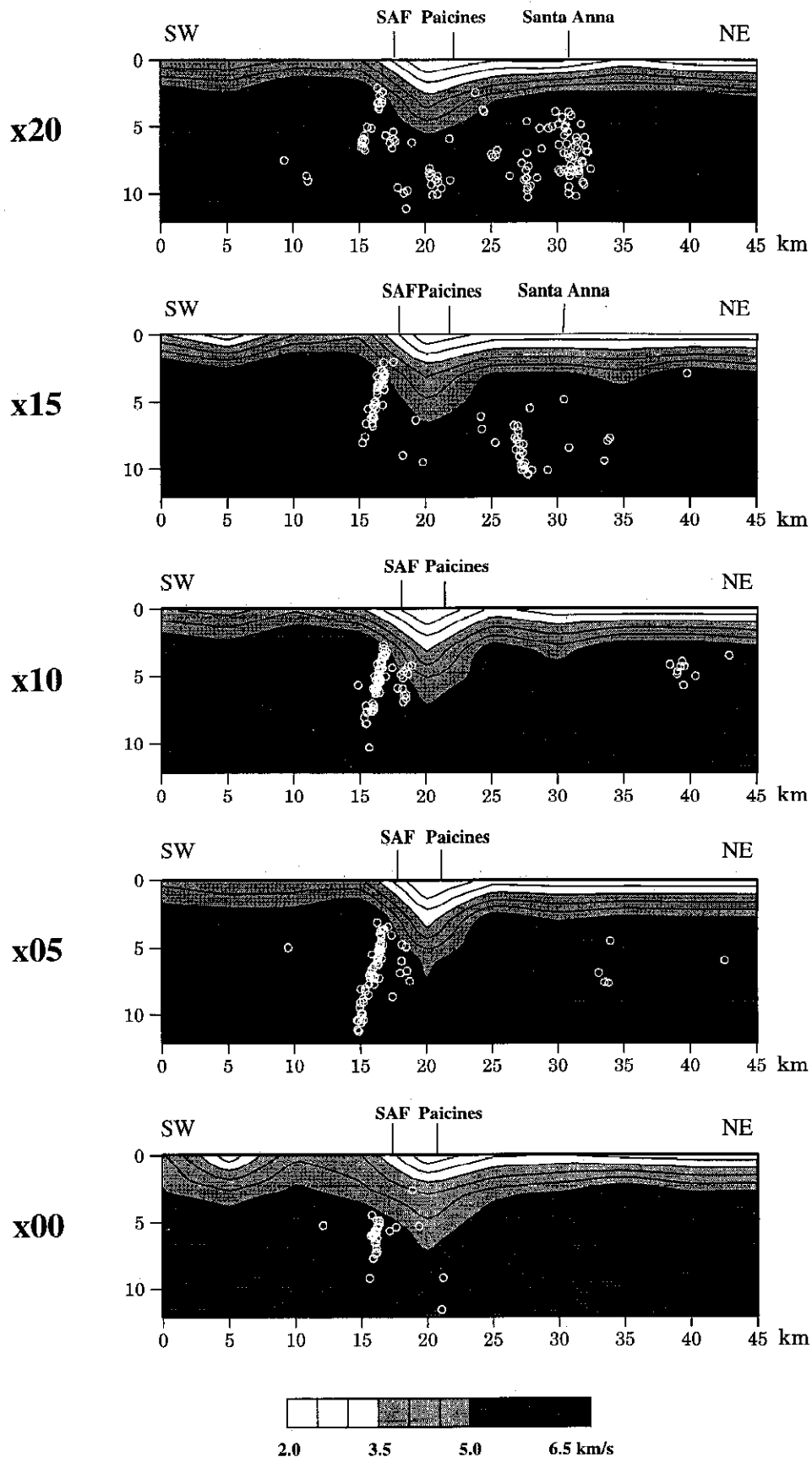**Figure 7b.** Same as Figure 7a, except sections x45 to x25.

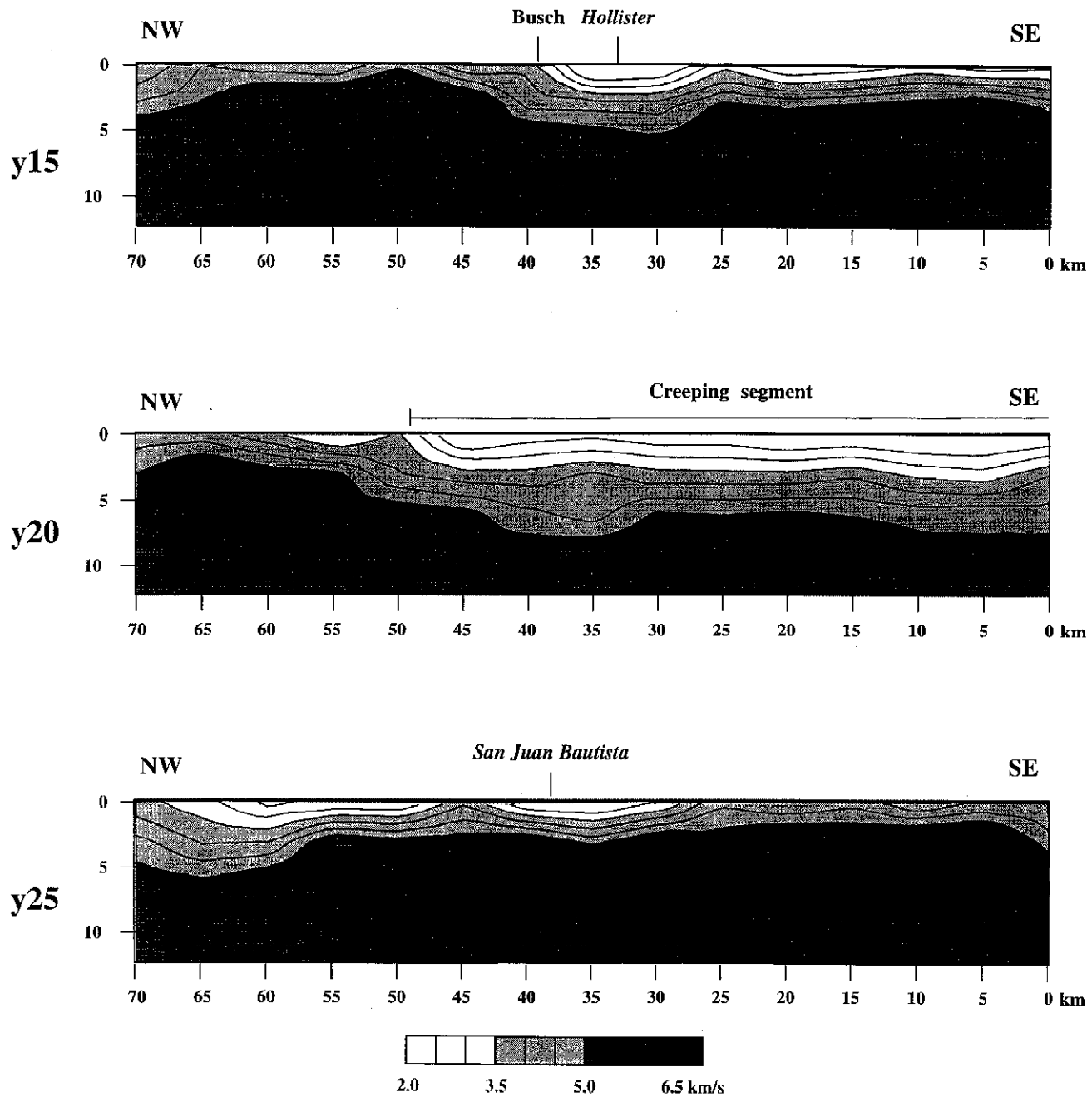Figure 7c. Same as Figure 7a, except sections x20 to x00.

Figure 7d. Cross sections parallel to the fault, sections y15 to y25.

In general, our velocity model compares favorably with previous studies, which partially span our study area but which may have used different analysis methods, data sets, and grid spacing. Where differences do occur, they can generally be attributed to the greater resolution provided by our more extensive data set and our finer grid spacing. In addition to the inversion stability tests discussed above, these results give us further cause to believe that the longer-wavelength features we observe are indeed reliable and that many of the shorter-wavelength features may also be significant.

Earthquake locations. Intuitively, the hypocenters based on a 3-D velocity model should yield an improvement over a 1-D model location. Yet some aspects of the inversion and modeling warrant closer scrutiny. In particular, the

approximate ray tracing (ART) through strong lateral velocity gradients may be inadequate.

First, we tested the convergence of our inversion algorithm. Based on the different local velocity models in Figure 3 and table 1 and the ART technique, we calculated synthetic travel times ("syn times") for the 1445 original NCSN hypocenters (the standard U.S. Geological Survey (USGS) locations). These syn times were then inverted to recover the input structure and input hypocenters.We used the 1-D NCG velocities at our 70x45x12 km^3 area grid points together with the 1445 USGS locations as a starting parameter set. The test velocity structure (Figure 3 and Table 1) and hypocenters were properly recovered. However, a few changes are observed, except along the southern part of the San Andreas fault. These latter
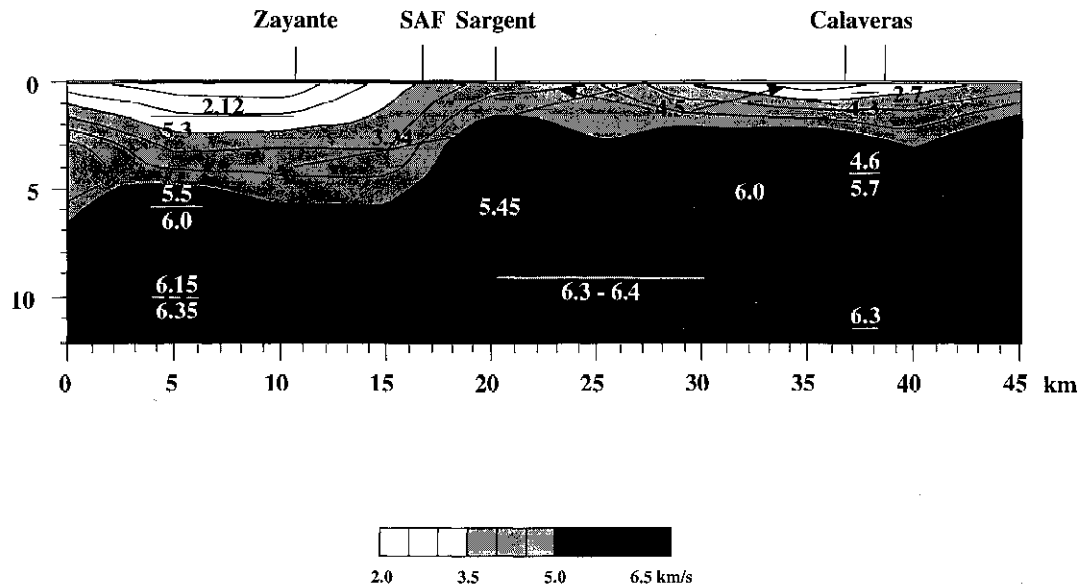
Figure 8. Superimposition of our cross section x65 (Figure 7a) and transect C2 [*Saleeby*, 1986; *Fuis and Mooney*, 1990]. Abbreviations are: Calaveras, Calaveras fault; SAF, San Andreas fault; Sargent, Sargent fault; Zayante, Zayante fault.

epicenters, which are systematically shifted by 2 km to the southwest on map view, were located with the GAB velocity model. Of the 1200 other events, 99% have been shifted by less than 1 km horizontally and 93% less than 1 km vertically. Cross sectional views BB' to HH' (Figure 9) show that the synthetic relocations have essentially the same pattern and dip as the original data. Cross section AA' in the Bear Valley region also shows that the hypocenters fall onto a plane which has the same near vertical dip as the original locations but is shifted to the southwest. Since the NCSN locations are determined from different models chosen according to where the earthquakes locate, it is not surprising that a single 3-D model should reproduce exactly the same results. This test suggests that the locations resulting from the inversion procedure are converging to the same location, regardless of the initial model used in the inversion. *Aki and Lee* [1976] reached a similar conclusion in their tomographic study of the Bear Valley region.

Suspecting ART technique errors in absolute location in regions with strong lateral heterogeneities, C.H. Lin and S.W. Roecker (preprints, 1994) applied an analytic ray-tracing technique in the study of the Bear Valley region. After relocation, they observed a shift of 772 events by 0-4 km southwest. Their relocated section defines a plane dipping 80° to the southwest, almost exactly the same result that we obtain in our study, which we discuss above. The similarity of their results to ours in the Bear Valley region where the lateral velocity changes are very large suggests that the offset of the hypocenters from the San Andreas fault is not due to the method of ray tracing used.

While the above two tests indicate that the locations are independent of the initial model or ray-tracing method, they do not preclude the possibility that the absolute locations may be systematically biased. The reliability of the earthquake locations can be independently assessed by analyzing focal mechanisms of strike-slip earthquakes occurring on a vertical fault separating rocks of different velocities. For these events the ray path of the first energy to arrive at seismic stations

situated on the "slow" side of the fault may be laterally refracted from the faster side of the fault rather than traveling the shortest-distance ray path through the slower medium. If the ray-tracing method does not properly model laterally refracted energy, then the ray parameters will be incorrect, and the observed first motions will "plot" in the wrong location on the focal sphere. Thus stations with large numbers of discrepant first-motion readings near the fault may indicate that the ray parameters are incorrect and, consequently, that the absolute locations may be systematically biased. Comparing the incompatible polarity readings for the USGS model to the new model, we note that there is no improvement. Thus our new model is not demonstrably better and leaves open the possibility that both the earlier model and our new model have ray path errors. The errors may be due to random errors in the identification of first motions, but this is thought to be unlikely.

To illustrate how the 3-D tomographic locations could be biased by unmodeled laterally refracted waves, we compute double-couple focal mechanisms for all earthquakes which have at least 40 first-motion readings using a grid-search algorithm [*Reasenberg and Oppenheimer*, 1985]. In Figure 10a we plot the locations of 878 earthquakes for which we computed focal mechanisms that are presumably occurring on the San Andreas fault. The 15 stations that have first-motion discrepancy rates which exceed 30% are situated between the San Andreas and Calaveras faults where, as we discuss above, the velocities are relatively low. By comparison, Figure 10b shows a subset of 489 earthquakes for the same time period but which occur east of the San Andreas and Calaveras faults. For this earthquake subset only one station, BSCM, exhibits a high discrepancy rate. This station also exhibits a high rate in Figure 10a, suggesting that its polarity may have been reversed due to faulty installation. The other 14 stations within the tomography region, however, exhibit systematic error rates in Figure 10a, indicating that lateral refraction in this region is the most likely problem.

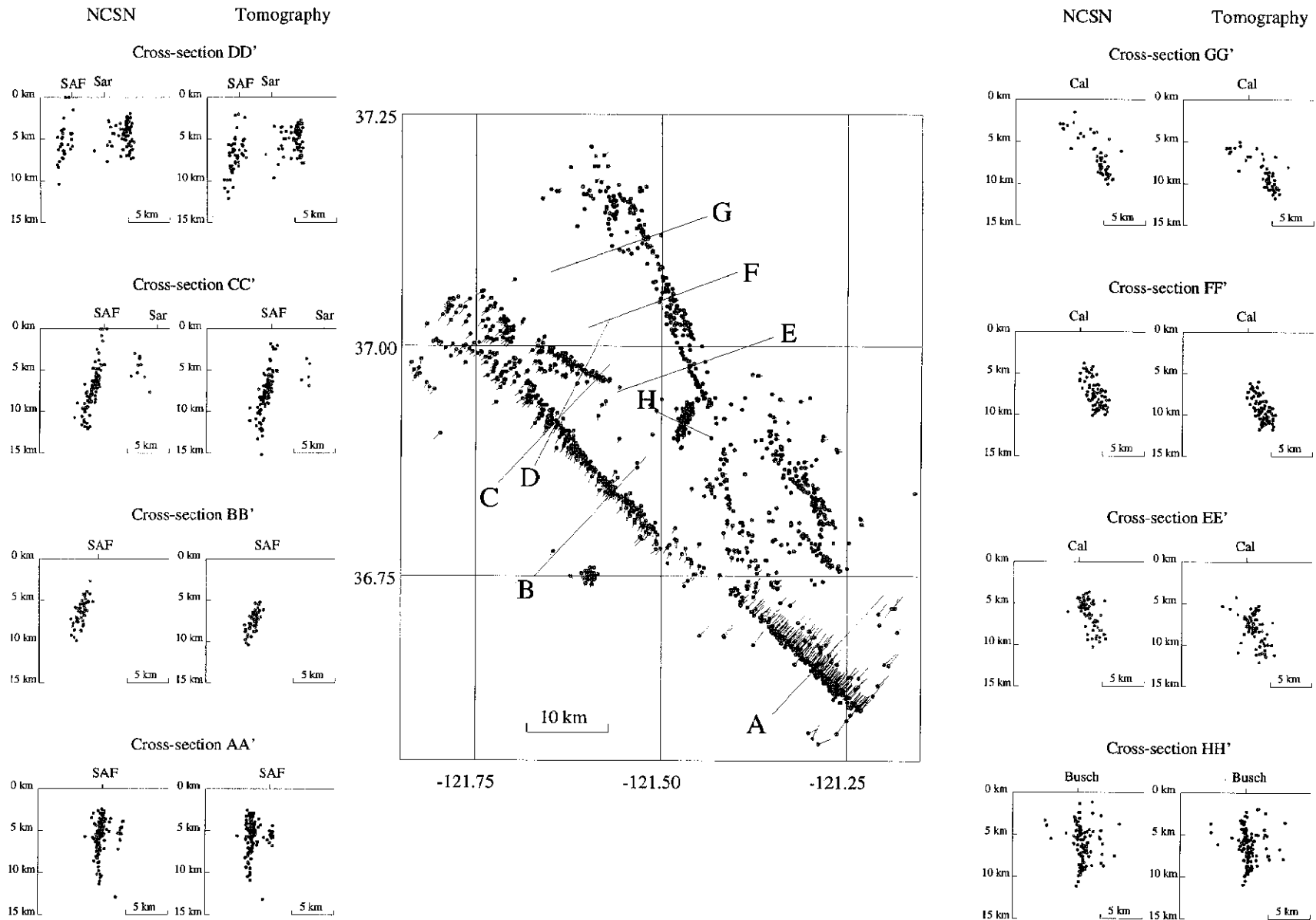In summary, we obtain the same 3-D velocity images from

Cross-section DD'

Cross-section CC'

Cross-section BB'

Cross-section AA'

Cross-section GG'

Cross-section FF'

Cross-section EE'

Cross-section HH'

37.25

37.00

36.75

10 km

-121.75   -121.50   -121.25

Figure 9. Same as Figure 6 but with locations resulting from tomographic inversion based on synthetic travel time data created from the NCSN locations with travel times computed using the multiple models. The initial locations for the inversion were determined with the synthetic travel times but with a different (NCG) velocity model. The NCG model was also the initial velocity model for the inversion.
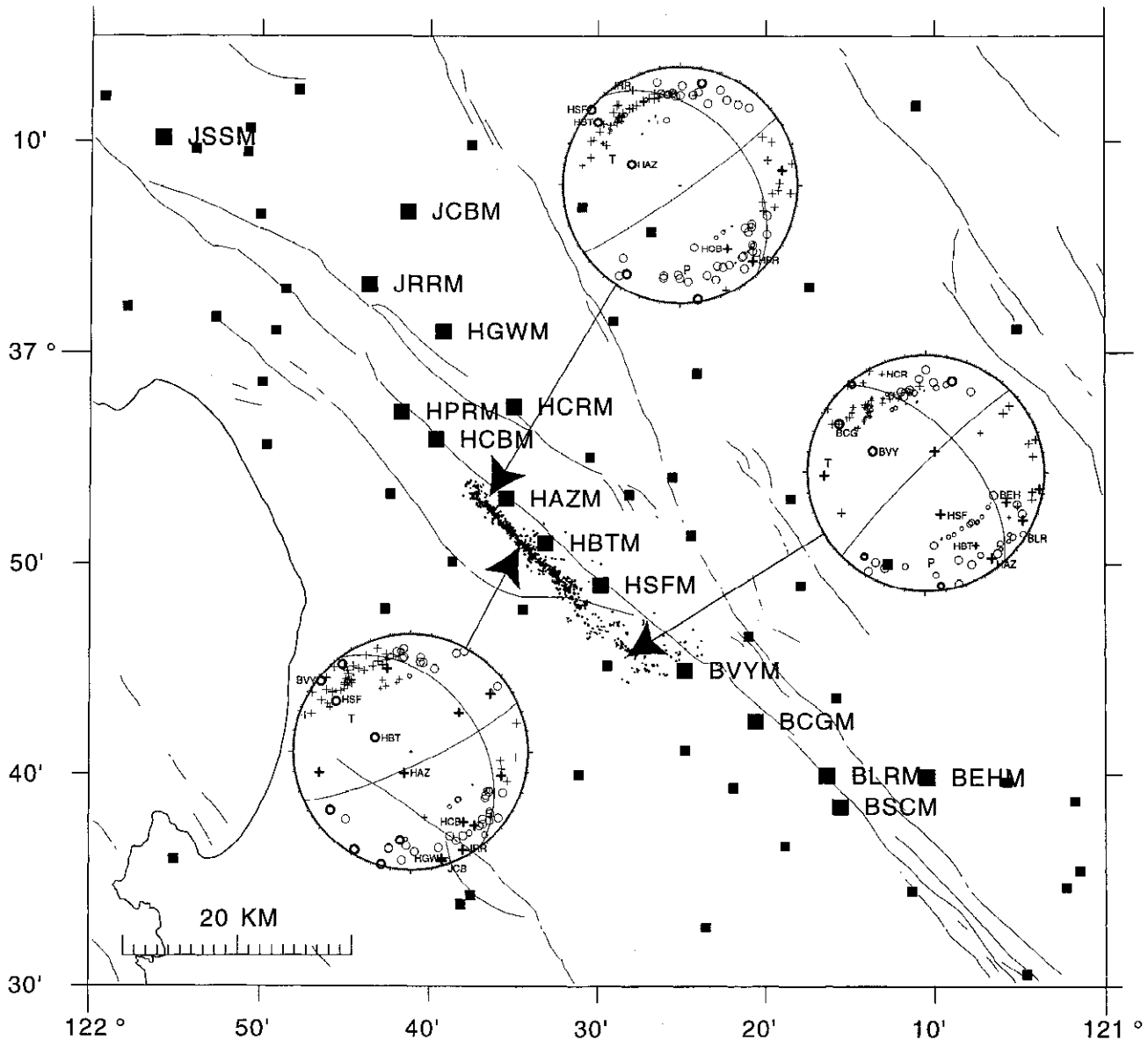
Figure 10a. Locations of earthquakes (small dots) relocated with the final 3-D velocity model and for which first-motion focal mechanisms were computed. Each mechanism had a minimum of 40 first-motion readings. Open circles and pluses represent dilatational and compressional first motions, respectively. Stations are denoted by squares. Labeled stations had first-motion readings which were inconsistent with the computed focal mechanism at least 30% of the time. For 878 earthquakes presumably occurring on the San Andreas fault, high discrepancy rates occur at 15 stations adjacent to the fault.

the tomographic inversion of travel times regardless of the initial velocity model. Though these images are stable, it should be noted that the resolution is not high everywhere and thus not all regions are equally reliable. Similarly, we obtain the same earthquake locations regardless of the 1-D or 3-D velocity model, ray trace algorithm, or location procedure, suggesting that the locations are stable. However, the first-motion data suggest that some calculated ray path parameters may be incorrect and hence the travel times may also be incorrect. If this error is a function path length, then the effect will be most pronounced for the deeper events and thus produce an artificial or exaggerated dip. We note later, however, that dips in the sense that we find (if not in magnitude) make sense geologically and for the deformation modelling.

Focal mechanisms. We computed focal mechanisms for all earthquakes with at least 40 P first-motion observations based on the ray parameters resulting from the 3-D relocations. We used a grid-search method [*Reasenberg and Oppenheimer*, 1985] that assumes a double-couple mechanism and weighs each observation by its reading quality and by the amplitude of radiation pattern. The median standard errors in strike, dip, and rake of the resulting set of 3771 mechanisms is 13°, 28°, and 25°, respectively. Because it is not reasonable to portray all of the data, we show representative mechanisms in map view (Figure 11).

A comparison of the mechanisms in Figure 11 with the trends in relocated seismicity indicates that the predominant style of deformation on the San Andreas, Calaveras, and
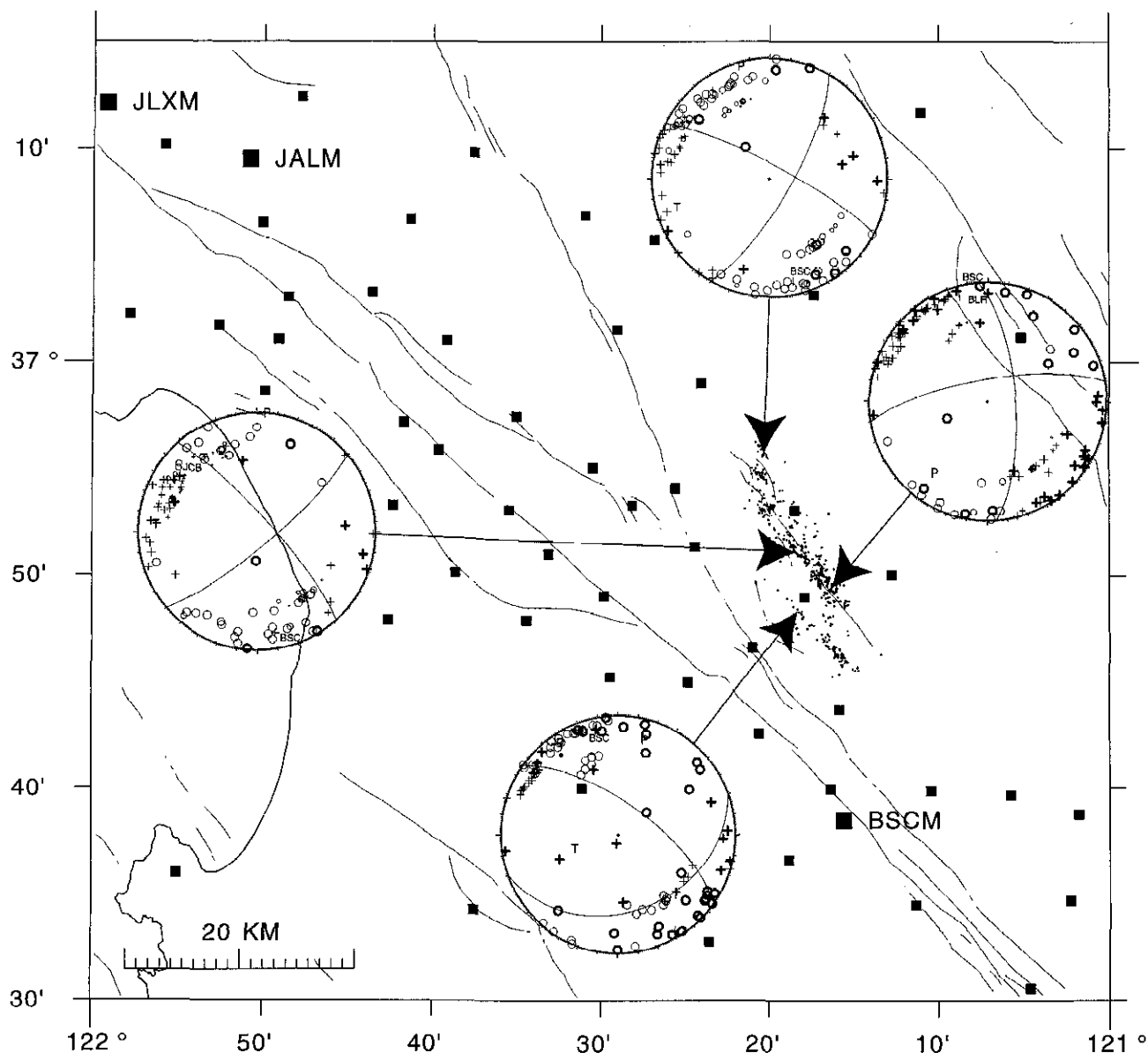
Figure 10b. For 489 earthquakes occurring east of the San Andreas fault during the same period of time, high discrepancy rates occur at only three stations. Mechanisms with first-motion plots illustrate position of discrepant observations on the focal sphere.

Sargent faults is predominantly right-lateral strike-slip on a near-vertical plane, as is well known. The mechanisms for earthquakes occurring on the Busch fault are left-lateral strike-slip on a vertical plane, as discussed by *Savage et al.* [1976]. Mechanisms and alignments of earthquakes occurring in the vicinity of the Quien Sabe fault show that deformation occurs by right-lateral, strike-slip motion on an echelon pattern of vertical faults with northwest and north orientations. Similar north oriented mechanisms as well as reverse mechanisms oriented parallel to the San Andreas system occur throughout the study region and likely reflect the fault-normal compressive stress that presumably arises due to a weak San Andreas fault [*Zoback et al.*, 1987].

The dips of selected focal mechanisms for earthquakes on the San Andreas fault do not align with the earthquakes, which dip 80° to the southwest. Instead, they tend to dip to the northeast. For mechanisms of 825 earthquakes occurring on

the San Andreas fault in vicinity of San Juan Bautista, the median dip is 61° to the northeast. Farther south in the Bear Valley region the dip of the focal mechanisms is bimodal; 41% have a median dip of 73° to the northeast. The remaining 59% of the mechanisms dip to the southwest 70°, 10° less than the observed alignment of hypocenters. Because the algorithm that computes the focal mechanism attempts to find a solution that minimizes the discrepancy between the predicted and observed first-motion data, the dip of the minimum solution can have a non vertical dip to be consistent with the first motions of refracted rays with incorrectly computed take off angles (Figure 6). Thus the near-vertical distribution of seismicity is probably a better indicator of fault orientation than are the individual focal mechanisms.

Relation between velocity and hypocenters. The fault segment ruptured by the Loma Prieta earthquake was almost completely aseismic before the earthquake and, unlike
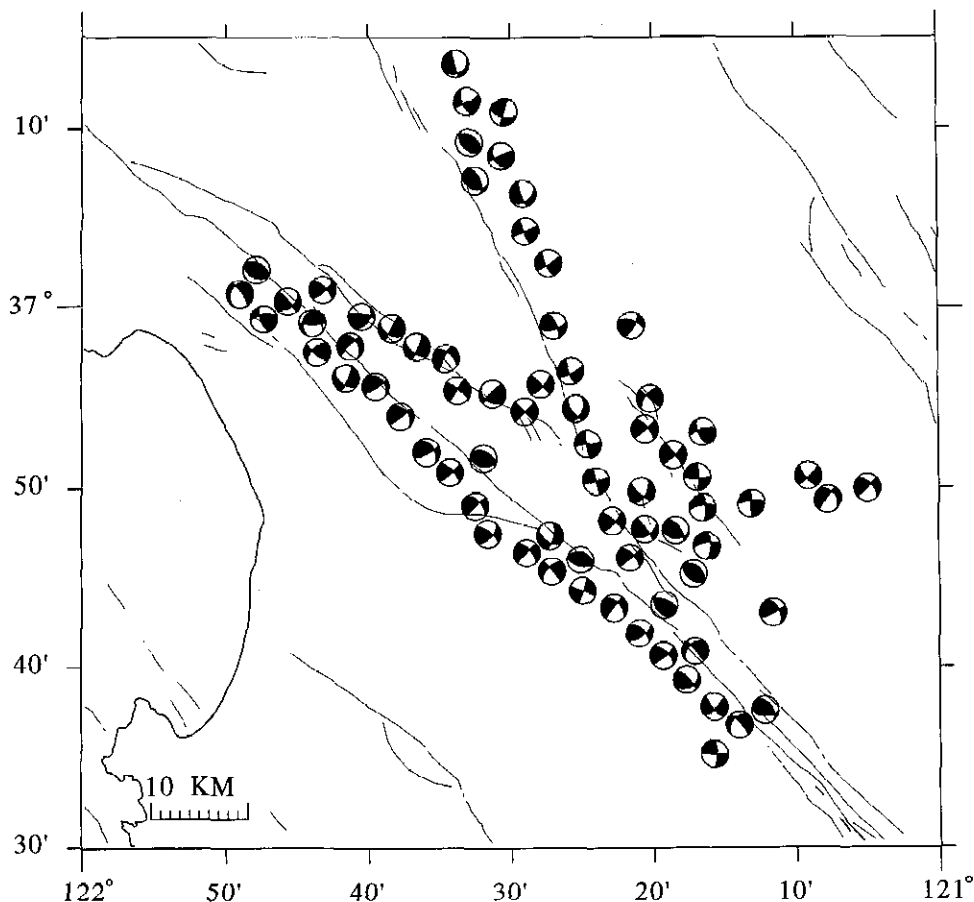
Figure 11. Representative first-motion focal mechanisms (lower hemisphere projection) of earthquakes located with 3-D velocity model. Quadrant containing T axis is darkened. These 72 mechanisms, chosen from a data set of 3771 earthquakes, have the greatest number of first-motion readings at their epicentral location. All mechanisms have a minimum of 40 first-motion readings. The first-motion data are shown for a few mechanisms to illustrate the distribution of data on the focal sphere.

the creeping section of the San Andreas fault to the south, was presumably locked. The quake also triggered numerous aftershocks on the creeping section of the San Andreas fault to the south of the rupture zone. The change in behavior from locked to creeping coincides with the northern end of the low-velocity wedge that extends into the Hollister valley (see also Figure 7d), a relation previously noted by *Thurber* [1983]. Similarly, the velocity model obtained using the Loma Prieta aftershocks [*Eberhart-Phillips et al.*, 1990] shows a difference between the mainshock zone and the creeping zone, where a sharp gradient is observed between high velocities to the west and low velocities to the east of the fault. A similar transition is observed at the southern end of the creeping segment of the San Andreas fault in the Parkfield region [*Eberhart-Phillips and Michael*, 1993]. *Michael and Eberhart-Phillips* [1991] suggested that the fault creeps where it is a well-developed structure and there is a contrast in material properties across the fault. Cross sections x45 to x0 (Figure 7) across the creeping segment of the San Andreas fault support these views. In this region, the fault is defined by a planar distribution of hypocenters with high velocities on the southwest side of the fault and slow velocities on the northeast.

Most hypocenters associated with the San Andreas fault locate where the velocity exceeds 5 km/s. This relation between seismicity and P wave velocity is particularly clear on

southern cross sections where the depth of the shallowest events increases as the velocity isolines become deeper. Earthquakes occurring on the Calaveras are also concentrated between 4 and 10 km in a zone where velocities vary from 5.5 to less than 6.5 km/s (Figure 7, x65 to x45). Such velocities correspond to the basement layer, which is presumably formed of Franciscan assemblage. No activity is observed in the upper layers presumably composed of Great Valley sequence rocks. This observation is similar to findings in other regions of California. The 1983 Coalinga mainshock ruptured a thrust fault within rocks of the Franciscan sequence $(5.7 < Vp < 6.2$ km/s). Rupture propagated up dip and terminated where Vp is less than 5.7 km/s, the inferred boundary between the Franciscan and the Great Valley sequence rocks [*Eberhart-Phillips*, 1989, 1990]. Similarly, most aftershocks of the 1984 Morgan Hill earthquake occurred in the Franciscan basement below the low velocity sedimentary rocks [*Michael*, 1988].

The same relation between the seismicity and rock type may also apply to other faults east of the San Andreas fault. In the Santa Anna valley region the seismicity occurs at depths greater than 4 km where the velocity is greater than 5.5 km/s (Figure 7, x30 to x20). Activity is only seen at depths between 3 and 10 km on the Quien Sabe fault where the velocities exceed 5.5 km/s (Figure 7, x20 and x15). Finally, seismicity
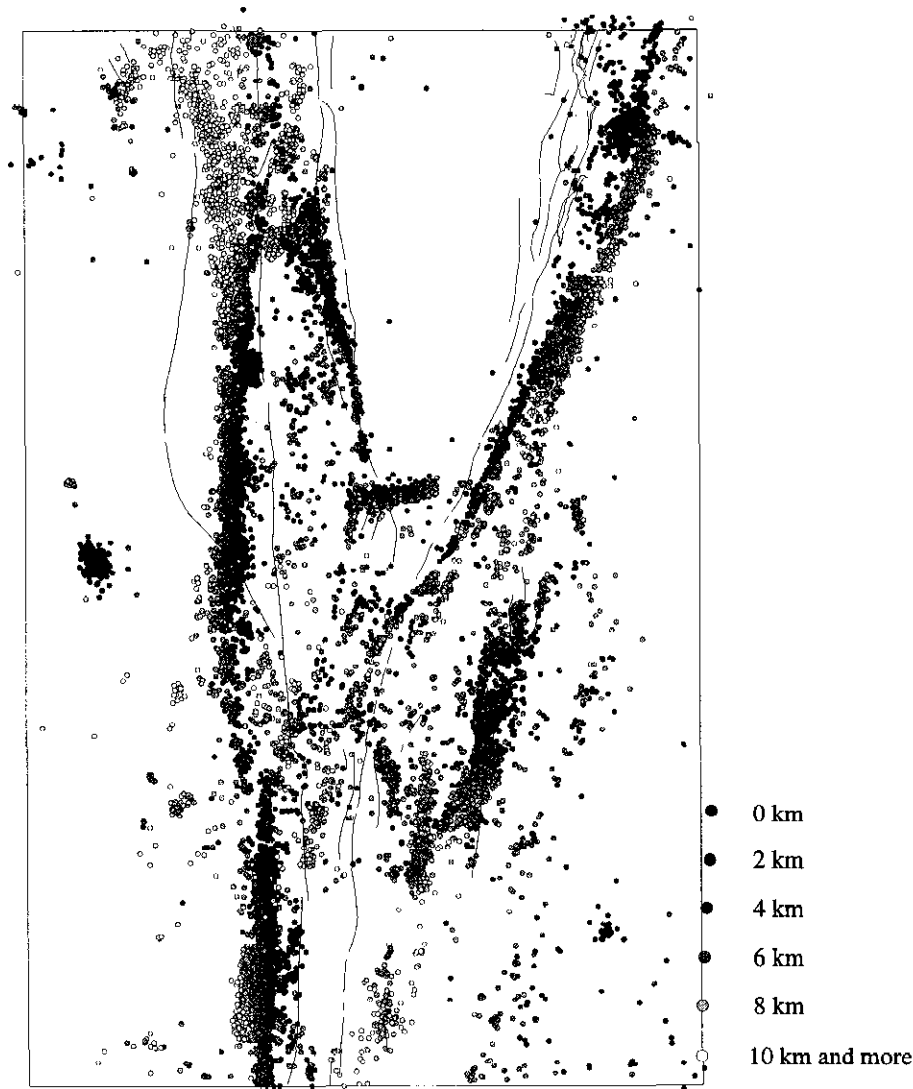
0 km

2 km

4 km

6 km

8 km

10 km and more

Figure 12a. Relocation of more than 17000 earthquakes with the final 3-D velocity model presented as an epicentral map. The epicentres have been shifted to the left such that when viewed together with Figure 12b they provide stereo image of the seismicity.

on the Sargent fault occurs between 3 and 9 km where the fault borders on the high-velocity Franciscan rocks to the southwest in the Santa Cruz mountains.

Topographic Modeling

Figure 12a shows all the events between 1967 and 1993 relocated with the final velocity model and presented as an epicentral map. To provide stereo image when viewed together, the epicenters in Figure 12a are shifted to the west linearly with depth. This is best carried out using a stereo viewer which is standard equipment in any good Earth science laboratory. Many of the features described above with the aid of the cross sections can be seen in three dimensions together with other interesting detail. The surface faults as mapped are also shown, and it is evident that the updip projection of the seismicity is almost everywhere consistent with the geologically mapped surface faulting. When viewing Figure 12 it should be remembered that seismicity near the borders of the region is not as well resolved as nearer to the centre.

Figure 12c shows a simplified version of the faulting consistent with the mapped traces and the seismicity. The surface expression of the faults is indicated by solid lines. Where the faults dip significantly, the location of the fault at 15 km depth is indicated by dashed lines, and in some places the numerical value of the dips are indicated. The deformation model described below approximates steeply dipping faults by equivalent vertical faults and it can be shown [Amelung, 1996] that these should lie close to the surface trace of the fault but offset in the dip direction. These are shown by thicker lines.

From a knowledge of the fault geometry and information about fault slip, it is possible to model regions of contraction and extension, which are assumed to reflect long-term uplift and subsidence. We cannot strictly model topography because some topography results from earlier phases of deformation with different fault geometries and slip rates. Nonetheless, comparing the regions of active uplift and subsidence predicted by this modeling with contemporary topography can provide insight into the tectonics of the region. Further discussion of this together with an examination of errors is given by
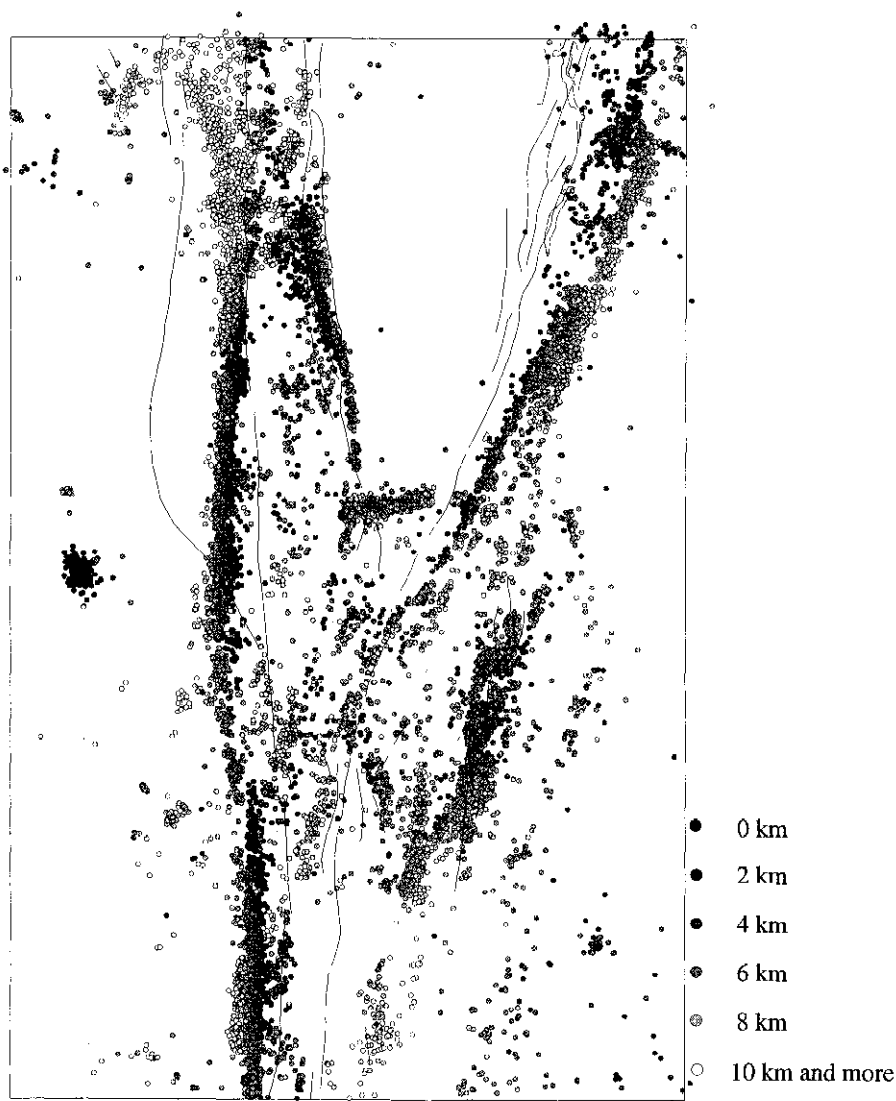
Figure 12b. Same as Figure 12a except not shifted.

Amelung [1996], and here we only discus that part relevant to interpreting the seismic data.

The basic technique is described by *Bilham and King* [1989] and *King et al.* [1993]. The specification of the fault geometry and the slip rates (Figure 12c) are based on the location of the mapped fault traces and the relocated seismicity. The model includes slip and fault geometries outside of the region imaged by tomography because modeling artifacts are introduced if the deformation is abruptly terminated at the edge of the region of interest. The slip rates are based on the work of *Kelson et al.* [1992] and *Lienkaemper et al.* [1991], but we have adjusted the rates within the reported error limits to achieve a better fit to the observed topography. The slip rates of the major faults, like the San Andreas and Calaveras, are prescribed. Minor faults, like the Sargent, Busch, and Quien Sabe (Figure 1), are incorporated in the model as free-slipping elements. This implies that slip on these faults reduces shear in the residual stress field due to the major faults.

The topography in the region of our seismic study (Figure 13a) shows two depressions. East of the San Andreas fault the Santa Clara valley broadens into the Hollister valley at its southern end. West of the San Andreas fault the Salinas valley broadens into a large depression at Monterey Bay. These depressions are divided by the northwest oriented Gabilan Range southeast of the San Andreas fault and the southern Santa Cruz Mountains where the Sargent fault intersects the San Andreas fault. The Diablo Range east of the San Andreas and Calaveras faults forms the eastern boundary to the Santa Clara and Hollister valleys.

A comparison of Figures 13a and 13b shows that many features of the topography can be explained by this simple deformation model. The overall form of the Hollister valley is reproduced together with subsidence extending toward Monterey Bay. Both regions are actively subsiding at present and thick deposits of Quaternary sediments, observed in the 3-D velocity structure, supports this view. Near Bear Valley, the model predicts uplift predominantly to the west of the fault. This is consistent with the current topography of the Gabilan Range, but the first-order topographic expression of the range is undoubtedly due to previous episodes of deformation. Similarly, the model predicts uplift of the Diablo Range in the northwest region of the tomographic study, but the uplift contribution from present orientation of faults is unknown.

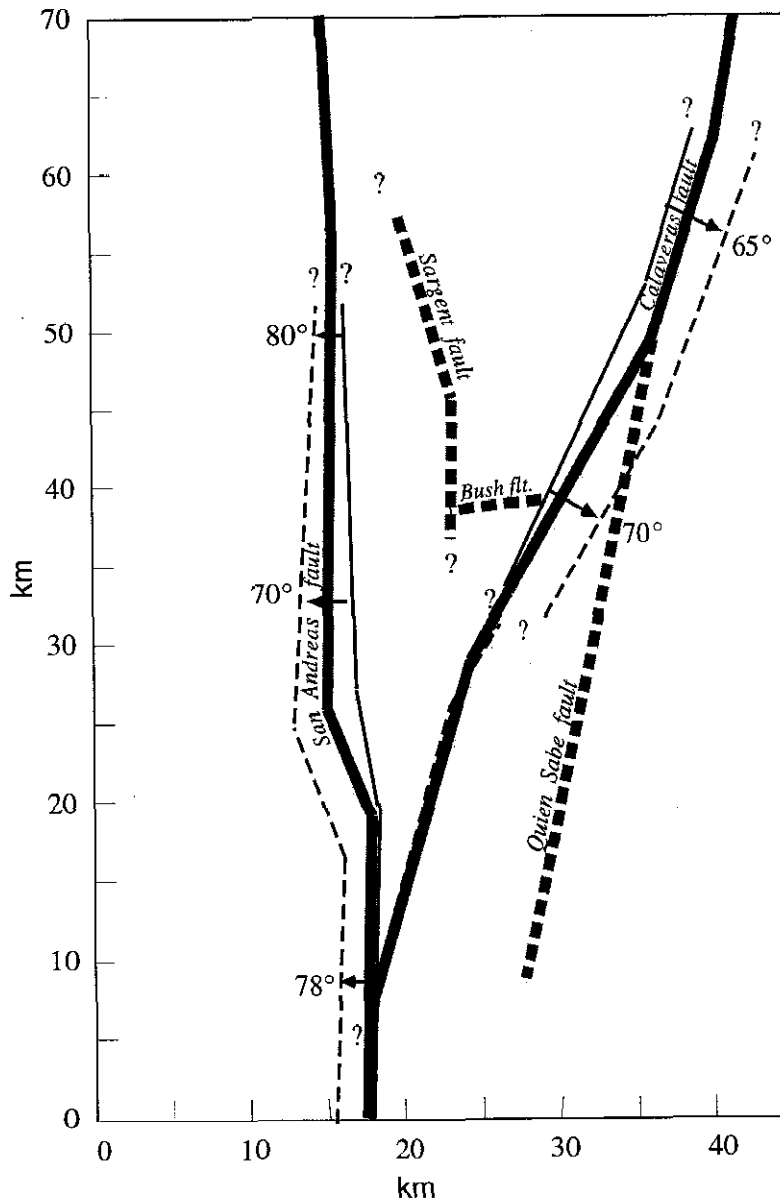Although the existence of the Hollister valley suggests that

Figure 12c. A simplified version of the faulting derived from geological information and examination of the stereo image. Solid thin lines represent surface fault expressions, and thin dashed lines the location of the same faults at a depth of 15 km where the dips are significant. Thicker solid lines show the positions of the faults used in the modeling and for which slips are defined. Dashed lines (Sargent, Busch, and Quien Sabe faults) show faults where slip has not been prescribed on the model but they have been allowed to slip freely in the response to deformation elsewhere. Their contribution to the final deformation is small.

the region is subsiding, the modeling predicts some local uplift near the city of Hollister. This results from the nearby change of dip of the San Andreas and the local bend in the Calaveras fault imaged by the tomographic modeling. Although no significant topographic features occur in the immediate vicinity of Hollister, there are a number of hills tens of meters in height (but not shown on Figure 13a) which may be of tectonic origin. The current fault geometry need not have persisted long to form these features. Considering the high slip rates, the fault orientations, and the absence of any expression of the uplift in the 3-D velocity results, we speculate that the intersection position of the San Andreas and

Calaveras faults changes with time and that its present detailed configuration was established recently.

The regions of compression and dilation found in the model together with information about fault dip from the 3-D model allow the sense of any dip-slip motion on the faults to be predicted. For the Calaveras north of the Hollister valley, this is overthrusting to the west, as observed. Where the fault enters the Hollister valley, however, the sense of dip-slip motion is predicted to reverse, and the fault is seen to acquire a small normal component down to the west. In Bear Valley the fault is overthrusting toward the east, but farther north near to Monterey Bay, the motion becomes normal downdropped to
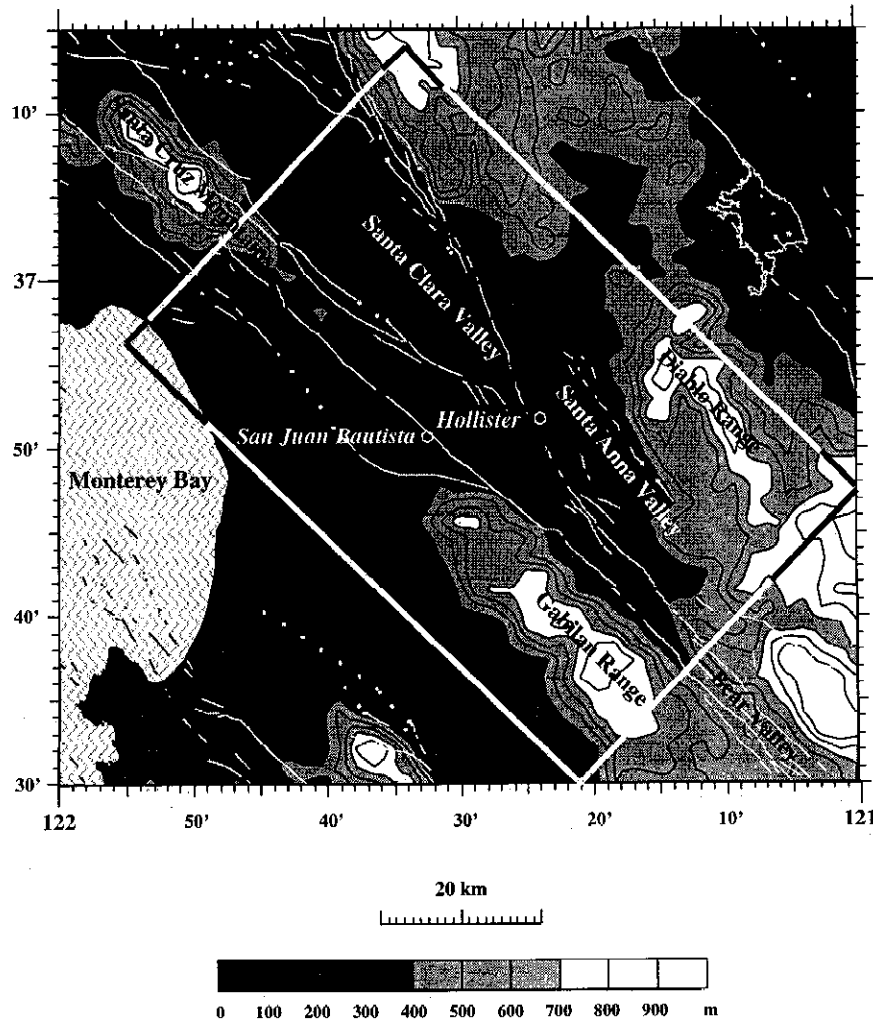
Figure 13a. Topographic relief of study region. Rectangle denotes 3-D modeling region. See Figure 1 for names of faults.

the west. Again these observations are consistent with the observed fault morphology.

Conclusions

Seismic tomography of the San Andreas and Calaveras fault junction reveals 3-D velocity to depths of 12 km. We observe significant velocity contrasts across creeping sections of both faults and find that relocated seismicity on the creeping sections generally occurs at depths where the P wave velocity exceeds 5.5 km/s. The velocity of the upper 3 km of the Hollister valley is less than 4.0 km/s, suggesting that the region is receiving sediments due to active subsidence. The northern boundary to this low-velocity region is clearly defined by the Sargent fault. North of the Sargent fault, velocities over comparable depths range from 5.0 km/s at the surface to 6.0 km/s at 3 km depth. The narrow region between the San Andreas and Paicines faults has velocities that are slow in comparison to the velocities of regions outboard of the two faults. The low velocities imaged in the northern Salinas valley to depths of 3 km are likely to reflect the deposition of sediments during the Quaternary.

A comparison of initial earthquake locations with those resulting from the tomographic inversion shows that the latter more closely define planes than before. In a number of cases, faults are found to dip at shallower angles than before. Because the first-motion data indicate that laterally refracted energy may not be fully modeled in the 3-D model, the fault dips may result from or be exaggerated by the 3-D ray-tracing method. The new dips when projected to the surface, however, produce a better correlation with the mapped surface faults than before.

From the fault geometry arising from the tomographic study and published estimates of fault slip rates we calculate the expected vertical deformation model for comparison with the present topography. Though significant topographic features in the region were likely to have been generated by faulting that is no longer active, some significant topographic features like the Hollister valley and the northern Salinas valley are predicted by the model. However, where the San Andreas and Calaveras faults diverge, small details of the predicted topography are not observed. We attribute this to small recent changes in the geometry of the triple junction. The broad overall agreement of the model topography with observed
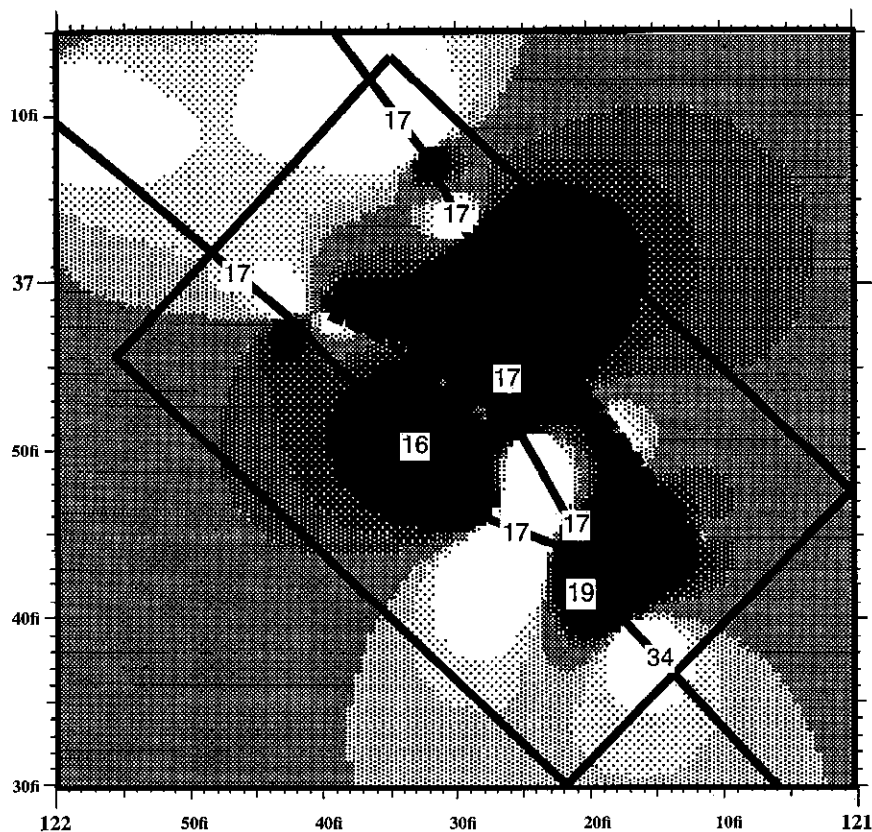
Figure 13b. Topographic modeling. Predicted areas of contraction (uplift) are shown in white, and areas of extension (subsidence) are shown in black. Simplified fault geometry is indicated by solid lines with given slip rates (mm/yr). Dashed faults are allowed to freely slip.

large-scale features, however, leads us to conclude that the present style of deformation has persisted for some time.

References

Aki, K., and W.H.K. Lee, Determination of three-dimensional velocity anomalies under a seismic array using first P arrival times from local earthquakes, 1, A homogeneous initial model, J. Geophys. Res., 81, 4381-4399, 1976.

Amelung, F., Kinematics of small earthquakes and tectonic deformation and topography in the San Francisco Bay area, Ph. D. thesis, 86 pp, Strasbourg Univ., Strasbourg, France, 1996.

Bilham, R., and G. King, The morphology of strike-slip faults: Examples from the San Andreas fault, California, J. Geophys. Res., 94, 10,204-10,217, 1989.

Blümling, P., and C. Prodehl, Crustal structure beneath the eastern part of the Coast Ranges (Diablo Range) of central California from explosion-seismic and near-earthquake data, Phys. Earth Planet. Inter., 31, 313-326, 1983.

Blümling, P., W.D. Mooney, and W.H.K. Lee, Crustal structure of the southern Calaveras fault zone, central California, from seismic refraction investigations, Bull. Seismol. Soc. Am., 75, 193-209, 1985.

Cockerham, R.S., and J.P. Eaton, The earthquake and its aftershocks, April 24 through September 30, 1984, in The Morgan Hill, California Earthquake of April 24, 1984,, edited by S.N. Hoose, U.S. Geol. Surv. Bull., 1639, 15-28, 1987.

Dietz, L.D., and W.L. Ellsworth, The October 17, 1989 Loma Prieta, California, earthquake and its aftershocks: Geometry of the sequence from high resolution locations, Geophys. Res. Lett., 17, 1417-1420, 1990.

Eberhart-Phillips, D., Active faulting and deformation of the Coalinga anticline as interpreted from three-dimensional velocity structure and seismicity, J. Geophys. Res., 94, 15,565-15,586, 1989.

Eberhart-Phillips, D., Three-dimensional P and S velocity structure in the Coalinga region, California, J. Geophys. Res., 95, 15,343-15,363, 1990.

Eberhart-Phillips, D., Local earthquake tomography: Earthquake source regions, in Seismic Tomography: Theory and Practice, edited by H.M. Iyer and K. Hirahara, pp. 613-643, Chapman and Hall, New York, 1993.

Eberhart-Phillips, D., and A.J. Michael, Three-dimensional velocity structure, seismicity, and fault structure in the Parkfield region, central California, J. Geophys. Res., 98, 15,737-15,758, 1993.

Eberhart-Phillips, D., V.F. Labson, W.D. Stanley, A.J. Michael, and B.D. Rodriguez, Preliminary velocity and resistivity models of the Loma Prieta earthquake region, Geophys. Res. Lett., 17, 1235-1238, 1990.

Ellsworth, W.L., Earthquake history, 1769-1989, in The San Andreas Fault System, California, edited by R.E. Wallace, U.S. Geol. Surv. Prof. Pap., 1515, 153-187, 1990.

Foxall, W., A. Michelini, and T.V. McEvilly, Earthquake travel time tomography of the southern Santa Cruz Mountains: Control of fault rupture by lithological heterogeneity of the San Andreas fault zone, J. Geophys. Res., 98, 17,691-17,710, 1993.

Fuis, G.S., and W.D. Mooney, Lithospheric structure and tectonics from seismic-refraction and other data, in The San Andreas Fault System, California, edited by R. Wallace, U.S. Geol. Surv. Prof. Pap., 1515, 207-236, 1990.

Hill, D.P., J.P. Eaton, and L.M. Jones, Seismicity, 1980-86, in The San Andreas Fault System, California, edited by R.E. Wallace, U.S. Geol. Surv. Prof. Pap., 1515, 115-151, 1990.

Kelson, K.I., W.R. Lettis, and M. Lisowski, Distribution of geologic slip and creep along faults in the San Francisco Bay region, in Proceedings of the Second Conference on Earthquake Hazards in the Eastern San Francisco Bay Area, edited by G. Borchardt et al., Spec.

Publ. 113, pp 31-38, Calif. Div. of Mines and Geol., Sacramento, 1992.

King, G.C.P., D. Sturdy, and J. Whitney, The landscape geometry and active tectonics of N.W. Greece, *Geol. Soc. Am. Bull., 105*, 37-161, 1993.

Klein, F.W., User's Guide to HYPOINVERSE, a program for VAX computers to solve for earthquake locations and magnitudes, *U.S. Geol. Surv. Open File Rep., 89-314*, 49 pp., 1989.

Lees, J.M., and E. Shalev, On the stability of *P*-wave tomography at Loma Prieta; A comparison of parameterizations, linear and nonlinear inversions, *Bull. Seismol. Soc. Am., 82*, 1821-1839, 1992.

Lienkaemper, J.J., G. Borchardt, and M. Lisowski, Historic creep rate and potential for seismic slip along the Hayward fault, California, *J. Geophys. Res., 96*, 18,261-18,283, 1991.

Michael, A.J., Effects of three-dimensional velocity structure on the seismicity of the 1984 Morgan Hill, CA aftershock sequence, *Bull. Seismol. Soc. Am., 73*, 1199-1221, 1988.

Michael, A.J., and D. Eberhart-Phillips, Relations among fault behavior, subsurface geology, and three-dimensional velocity models, *Science, 253*, 651-654, 1991.

Michelini, A., and T.V. McEvilly, Seismological studies at Parkfield, I, Simultaneous inversion for velocity structure and hypocenters using cubic B-splines parameterization, *Bull. Seismol. Soc. Am., 81*, 524-552, 1991.

Mooney, W.D., and R.H. Colburn, A seismic-refraction profile across the San Andreas, Sargent, and Calaveras faults, west-central California, *Bull. Seismol. Soc. Am., 75*, 175-191, 1985.

Oppenheimer, D.H., W.H. Bakun, and A.G. Lindh, Slip partitioning of the Calaveras fault, California, and prospects for future earthquakes, *J. Geophys. Res., 95*, 8483-8498, 1990.

Reasenberg, P., and W.L. Ellsworth, Aftershocks of the Coyote Lake, California, earthquake of August 6, 1979: A detailed study, *J. Geophys. Res., 87*, 10637-10655, 1982.

Reasenberg, P.A., and D.H. Oppenheimer, FPFIT, FPPLOT, and FPPAGE: FORTRAN computer programs for calculating and displaying earthquake fault-plane solutions, *U.S. Geol. Surv. Open File Rep., 85-739*, 109 pp., 1985.

Romanowicz, B., D. Neuhauser, B. Bogaert, and D. Oppenheimer,

Accessing northern California earthquake data via internet, *Eos Trans. AGU, 75*, 257-260, 1994.

Saleeby, J.B., Explanatory text for the continent-ocean transect: Corridor C2, Central California offshore to the Colorado Plateau, 63 pp., Calif. Inst. of Technol., Div.of Geol. and Planet. Sci., Pasadena, 1986.

Savage, J.C., M.A. Spieth, and W.H. Prescott, Preseismic and coseismic deformation associated with the Hollister, California, earthquake of November 28, 1974, *J. Geophys. Res.*, 81, 3567-3574, 1976.

Savage, J.C., W.H. Prescott, M. Lisowski, and N. King, Geodolite measurements of deformation near Hollister, California, 1971-1978, *J. Geophys. Res.*, 84, 7599-7615, 1979.

Simpson, R.W., The Loma Prieta, California, earthquake of October 17, 1989: Tectonic processes and models, *U.S. Geol. Surv. Prof. Pap., 1550-F*, 1-131, 1994.

Thurber, C.H., Earthquake locations and three-dimensional crustal structure in the Coyote Lake area, central California, *J. Geophys. Res., 88*, 8226-8236, 1983.

Thurber, C. H. Local earthquake tomography: velocities and *Vp/Vs* -Theory, in *Seismic tomography: Theory and Practice*, edited by H.M. Iyer and K. Hirahara, pp. 563-583, Chapman and Hall, New York, 1993.

Walter, A.W., and W.D. Mooney, Crustal structure of the Diablo and Gabilan ranges, central California: A reinterpretation of existing data, Bull. Seismol. Soc. Am., 72, 1567-1590, 1982.

Zoback, M.D., M.L. Zoback, V.S. Mount, J. Suppe, J.P. Eaton, J.H. Healy, D. Oppenheimer, P. Reasenberg, L. Jones, C.B. Raleigh, I.G. Wong, O. Scotti, and C. Wentworth, New evidence on the state of stress of the San Andreas fault system, Science, 238, 1105-1111, 1987.

F. Amelung, C. Dorbath, and G. King, EOPG, 5 rue René Descartes, 67084 Strasbourg Cedex, France. (e-mail: cath@mapu.u-strasbg.fr)

D. Oppenheimer, U.S. Geological Survey, 345 Middlefield Road, MS 977, Menlo Park, CA 94025. (e-mail: oppen@alum.wr.usgs.gov)